ISSN 0255-7193

CLAY RESEARCH

Vol. 38, No. 2

December 2019

IOS Press

Overseas distribution
IOS Press, The Netherlands

THE CLAY MINERALS SOCIETY OF INDIA
Division of Soil Science and
Agricultural Chemistry
Indian Agricultural Research Institute
New Delhi-110 012, India

Overseas subscribers may send
their queries to IOS Press, Nieuwe
Hemweg 6B, 1013 BG Amsterdam,
The Netherlands, orders@iospress.in:
URL: http://www.iospress.nl

THE CLAY MINERALS SOCIETY OF INDIA

(Registered under Act XXI of 1860)
Registration No. S/13028 of 1982

COUNCIL FOR 2019–20

President	:	Dr. S.C. Datta
Vice Presidents	:	Dr. Nayan Ahmed; Dr. P. Chandran
Secretary	:	Dr. S.K. Mahapatra
Joint Secretaries	:	Dr. Gautam Goswami; Dr. Saumitra Das
Treasurer	:	Ms. Ritu Nagdev
Chief Editor	:	Dr. Siddhartha S. Mukhopadhyay
Editors	:	Dr. K. M. Manjaiah; Dr. D.C. Nayak; Dr. S.K. Roy
		Dr. P. Chandran; Dr. Somsubhra Chakraborty
Councilor	:	East Zone : Dr. Siladitya Bandyopadhyay, Dr. Prasenjit Roy
	:	West Zone : Dr. P. Chandran; Dr. D. Raja
	:	North Zone : Dr. U.K. Maurya, Dr. T. Satyanarayana
	:	South Zone : Dr. Anil Kumar K.S.
	:	Central Zone : Dr. Vassanda Coumar, Dr. Ranjan Paul
Past Presidents	:	Dr S.K. Mukherjee, Dr K.V. Raman, Dr S.K. Ghosh,
		Dr. D.K. Pal, Dr. Dipak Sarkar, Dr. Kunal Ghosh, Dr. S.K. Singh

INTERNATIONAL EDITORIAL CONSULTANT

International Consulting Editor	:	Dr. S.R. Krishnamurti Gummuluru Adjunct Associate Professor, CERAR, University of South Australia, Canada Dr. Sridhar Komarneni Adjunct Professor of Civil and Environmental Engineering & Editor-in-Chief, J. Porous Materials, USA

Annual Institutional Subscription Rates Inclusive of Air Mail and Handling Charges :

Subscription Rates (Year 2011)	Indian (INR)	Overseas (USD)
Print + online access	Rs. 1,800.00	$ 350.00
Online access	Rs. 600.00	$ 150.00
Print	Rs. 1,200.00	$ 200.00

All payments should be sent to **"The Clay Minerals Society of India"** Division of Soil Science and Agricultural Chemistry, I.A.R.I., New Delhi-110 012

Clay Research, Vol. 38, No. 2, pp. 43-55 (2019)

Covid-19 and Nanoform Zinc Oxide Interaction: A Forcite Module of Materials Studio Software Study

R. DJEFAFLIA [1,2,3] D. LERARI [1] AND K. BACHARI [1]

[1] *Scientific and Technical Research Center in Physicochemical Analysis, BP 384, Bou-Ismail Industrial Zone, RP 42004, Tipaza, Algeria.*
[2] *Faculty of Science and Technology, Mohamed Cherif Messaadia University, B.P 1553 Souk-Ahras, Algeria*

[Znic oxide is a commonly occurring mineral in soils. Soil is also ultimate sink for engineered nano-ZnO. In view of Covid-19 Pandemic and that nano-ZnO is reported to have damaged or destroyed genetic make-ups in living cells in plants, this paper has been commissioned to explore the potential use of nano-ZnO to control the virus by destroying its genetic structure – Chief Editor]

Abstract *– In this article, by using the Forcite module of Materials Studio software, we studied the interactions between ZnO as a magic material because of its versatile applications, where the Zinc oxide NPs are used in biomedicine like biomedical imaging, drug delivery, gene delivery, and bio sensing potential, On the other hand, nano-ZnO is reported to have damaged or destroyed genetic make-ups in living cells in plants; and Alanine because it is one of the 20 amino acids mainly present in the peptide chains of proteins, and because of its exceptional properties, in the goal of knowing their interactions to estimate the interactions of ZnO with the coronavirus. The results of geometric optimization showed that there are very strong interactions between ZnO and Alanine where the structure of ZnO got distorted by releasing Zn^{2+} ions. The release of Zn^{2+} ions in the middle of proteins Leads to the Zinc fingers. The abundance of Zn^{2+} ions in the medium of proteins leads to the abundance of proteins of Zinc fingers, which have a lot of influence on the proteins and its structures apart from a few more advantages. We conclude that the interactions of ZnO with proteins could find a way to destroy viruses, especially novel coronavirus (Covid-19).*

Keywords: Alanine; Coronavirus; nanotechnology; nano-zinc; Protein Data Bank; zinc fingers; ZnO nanoparticles

Nanotechnology has revolutionized the commercial application of nano sized minerals in the fields of medicine, engineering, information, environmental technology pigments, food, electronics appliances, biological and pharmaceutical applications and many more. This is also been used as a recent tool in the fields of biology (molecular and cellular), biotechnology, mineral nutrition, physiology, reproduction, pharmacology etc, in both animal and human models. Furthermore, it can be used for pathogen detection. Thus, there are diversified areas and use of nanotechnology including the science and engineering of agriculture, animal and food systems (Swain *et al.*, 2016).

Recently, biomedical nanomaterials have received more concerns because of their prominent biological characteristics and biomedical applications. With the development of nanomaterials, metal oxide nanoparticles show promising and far-ranging prospect for

[3]**Corresponding Author's E-mail:** samira.djefaflia@yahoo.com
DOI: 10.5958/0974-4509.2019.00001.9

biomedical field, especially for antibacterial, anticancer drug/gene delivery, cell imaging, biosensing, and so on (Mishra *et al.,* 2017)

Among metal nanoparticles (NP) annually produced, by volume, nano zinc oxide (nZnO) is the third highest globally produced nano metal after nano SiO_2 and nano TiO_2 (Piccinno et al., 2012). The sudden rise in the demand in zinc oxide nanoparticles (ZnO NP) is mostly attributed to its better antibacterial properties than the conventional ZnO (Padmavathy et al., 2008).

Zinc Oxide is considered to be a magic material because of its versatile applications. Zinc oxide NPs are used in biomedicine like biomedical imaging, drug delivery, gene delivery, and bio sensing potential (Zhang *et al.,* 2013). The ZnO is used in ceramics, as filler in rubber and plastics, cosmetics, electrical and optoelectronic devices, and pigments (Srivastava *et al.,* 2012). ZnO NPs less than 100 nm are considered to be relatively biocompatible, which support their biomedical applications and represent a powerful property in promoting the biomedical research.

Zinc oxide NPs, as a new type of the low-cost and low-toxicity nanomaterial, have attracted tremendous interest in various biomedical fields, including anticancer, antibacterial, antioxidant, antidiabetic, and anti-inflammatory activities, as well as for drug delivery and bioimaging applications (Rasmussen, *et al.,* 2010 ; Zhang, *et al.,* 2015 ; Kim, *et al.,* 2017 ; Xiong, 2013).

Zinc oxide NPs have emerged a promising potential in biomedicine, especially in the fields of anticancer and antibacterial fields, which are involved with their potent ability to trigger excess reactive oxygen species production, release zinc ions, and induce cell apoptosis. In addition, zinc is well known to keep the structural integrity of insulin. So, ZnO NPs also have been effectively developed for antidiabetic treatment. Moreover, ZnO NPs show excellent luminescent properties and have turned them into one of the main candidates for bioimaging (Jiang, *et al.,* 2018).

Despite all this technology and innovation in the field of medicine and nanoscience, the science remains powerless in front of the coronavirus which threatens the world and humanity.

In recent times, several life threatening viruses have emerged. They have been responsible for causing significant human mortality, in addition to raising serious public health concerns worldwide. The coronaviruses represent a global threat that does not recognize international borders. Coronaviruses are enveloped viruses responsible for up to 30% of mild respiratory tract infections and atypical pneumonia in humans.

Coronaviruses infect birds and many mammals, including humans. The respiratory tract, gastrointestinal organs, and neurological tissue are the most common targets for coronaviruses, but other organs including the liver, heart, kidneys, and eyes may also be affected (Escor *et al.,* 2001 (a, b)). Epithelial cells are the main targets of coronaviruses (Alonso *et al.,* 2002 (a, b)). Widely distributed cells such as macrophages are also often infected with coronaviruses.

Coronavirus is an enveloped positive-sense RNA virus, which is characterized by club-like spikes projecting from its surface. Although coronavirus is commonly associated with acute respiratory infections in humans, its ability to infect multiple host species and a variety of diseases makes it a complex pathogen (Fung *et al.,* 2019). The frequent interactions of wild animals with humans make them a common source of zoonotic infections. Severe Acute Respiratory Syndrome Coronavirus (SARS-CoV) and Middle Eastern Respiratory Syndrome Coronavirus (MERS-CoV) are zoonotic pathogens that can cause severe respiratory diseases in humans (Luk *et al.,* 2019; Ramadan *et al.,* 2019). CoVs are members of two subfamilies: Coronavirinae and Torovirinae, from

the family Coronaviridae, hich in turn is from the order Nidovirales (De Groot, 2011).

The Coronavirinae subfamily is further classified into four main genera: a-coronavirus, b-coronavirus, g-coronavirus and d-coronavirus, based on the International Committee for Taxonomy of Viruses. HCoV-229E and HCoV-NL6 belong to the á-coronavirus, HCoV-HKU1, SARSCoV, MERS-CoV and HCoV-OC43 are â-coronaviruses, and both genera infect only mammals. ã-Coronavirus and ä-coronavirus mostly infect birds, but some can infect mammals as well (Woo, *et al.,* 2012). Based on current sequence databases, it has been discovered that all human CoVs have animal origins: SARS-CoV, MERS-CoV, HCoV-NL63 and HCoV-229E are considered to have originated in bats; HCoV-OC43 and HKU1 probably originated from rodents (Su, *et al.,* 2016, Forni, *et al.,* 2017).

The coronaviral genome encodes four major structural proteins: the spike (S) protein, nucleocapsid (N) protein, membrane (M) protein, and the envelope (E) protein, all of which are required to produce a structurally complete viral particle (Masters, *et al.,* 2006, Mortola, *et al.,* 2004, Wang, *et al.,* 2017). More recently, however, it has become clear that some CoVs do not require the full ensemble of structural proteins to form a complete, infectious virion, suggesting that some structural proteins might be dispensable or that these CoVs might encode additional proteins with overlapping compensatory functions (DeDiego, *et al.,* 2007, Mortola, *et al.,* 2004, Kuo, *et al.,* 2003, Ortego, *et al.,* 2007, Ruch, *et al.,* 2012, Siu, *et al.,* 2008). Individually, each protein primarily plays a role in the structure of the virus particle, but they are also involved in other aspects of the replication cycle.

The replication of CoV begins with the binding of its spike protein (S) on the cell-surface molecules of the host. This receptor recognition is important for initiating virus entry into the host cells, thereby playing a major part in the tissue and host species tropism of viruses. The receptors used by all human CoVs are known: aminopeptidase N by HCoV-229E (Yeager, *et al.,* 1992); 9-Oacetylated sialic acid by HCoV-OC43 and HCoV-HKU1 (Huang, *et al.,* 2015, Butler, *et al.,* 2006]; angiotensin-converting enzyme 2 (ACE2) by SARS-CoV (Li, *et al.,* 2003); and HCoV-NL63 (Li, *et al.,* 2007, Wu, *et al.,* 2009) and dipeptidyl peptidase 4 (DPP4) by MERS-CoV (van Doremalen, *et al.,* 2014).

Members of the Coronaviridae family infect a wide range of animal species in nature and most are limited in their host range (Masters, *et al.,* 2013). Human coronaviruses including OC43, 229E, NL63 and HKU1 are generally associated with self-limiting respiratory tract infections (Masters, *et al.,* 2013, Gralinski, *et al.,* 2015). However, in the past 12 years, two outbreaks of severe respiratory tract infection, SARS and

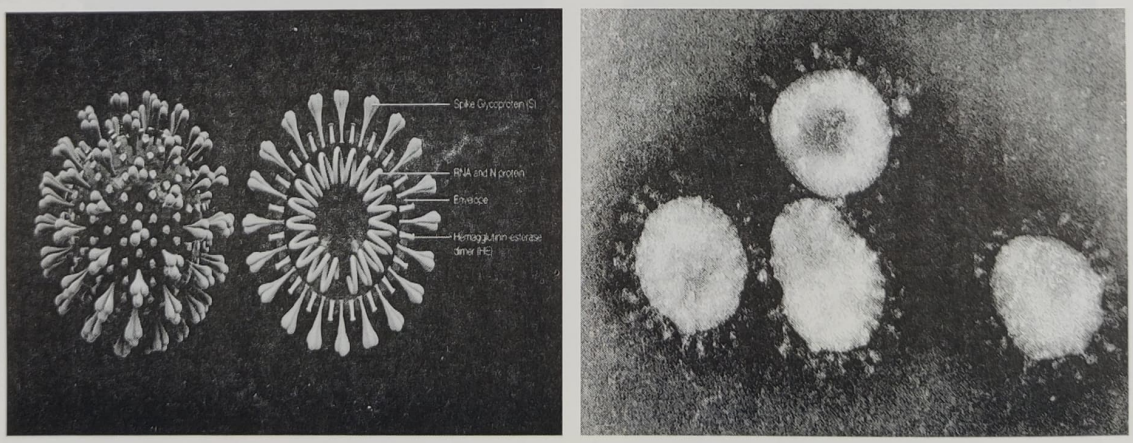

Fig. 1. *Medical animation of coronavirus and coronavirus microscopic photo respectively.*

MERS, have been caused by animal coronaviruses that have crossed the species barrier. Despite the severe disease and high case fatality rate associated with SARS and MERS, coronavirus vaccines and antiviral drugs are not yet available.

The workers have characterized the presentation of Middle East Respiratory Syndrome (MERS) (Al-Tawfiq, *et al.,* 2017) and Severe Acute Respiratory Syndrome (SARS) (Lim, *et al.,* 2004) to aid clinical teams in the recognition, diagnosis and management of these cases. Now with the emergence of a novel coronavirus (CoV) from Wuhan, China (tentatively named as 2019-nCoV by The World Health Organization – WHO), (Lu, *et al.,* 2020, Bogoch, *et al.,* 2020) similar clinical, diagnostic and management guidance are required.

In view of this problem of this virus which threatens humanity and the world, and according to the efficacy of ZnO nanoparticles in the medical field, we have made a theoretical study on the interactions between ZnO and Alanine, because Alanine is one of the 20 amino acids mainly present in the peptide chains of proteins, where the corona virus attacks living cells which are made up of amino acids and proteins.

We used Materials Studio 7.0 simulation software for this modeling.

Materials Studio is now being used effectively over more than a decade for numerous different applications across a range of physical and chemical sciences and almost every industrial sector (Reinier *et al.,* 2015). Materials Studio Forcite is an advanced classical molecular mechanics tool that allows fast energy calculations and reliable geometry optimization of molecules and periodic systems (Accelrys Software Inc. 2012). The Forcite simulation was performed the interaction between ZnO and the Alanine as a protein.

Materials and Methods

Geometry optimization of all the prepared models was carried out in Materials Studio 7.0 software (Materials Studio. Accelrys Software Inc., San Diego., 2013) under the Forcite module (Accelrys Software Inc. 2012), using the Universal Force Field (Rappé *et al.,* 1992). We started by investigating the ZnO in the lattice 3D hexagonal, where the crystallographic parameters for the single cell are α = 0.324 nm, b = 0.324 nm, c = 0.520 nm and $\alpha = \beta = 90°$, $\gamma = 120°$ (Fig. 2a).

In our study, for best optimization we must build super cell of ZnO. For the new super cell (3x3x3), the parameters are a = 0.974 nm, b = 0.974 nm, c = 1.561 nm and $\alpha = \beta = 90°$, $\gamma = 120°$ (Fig. 2b).

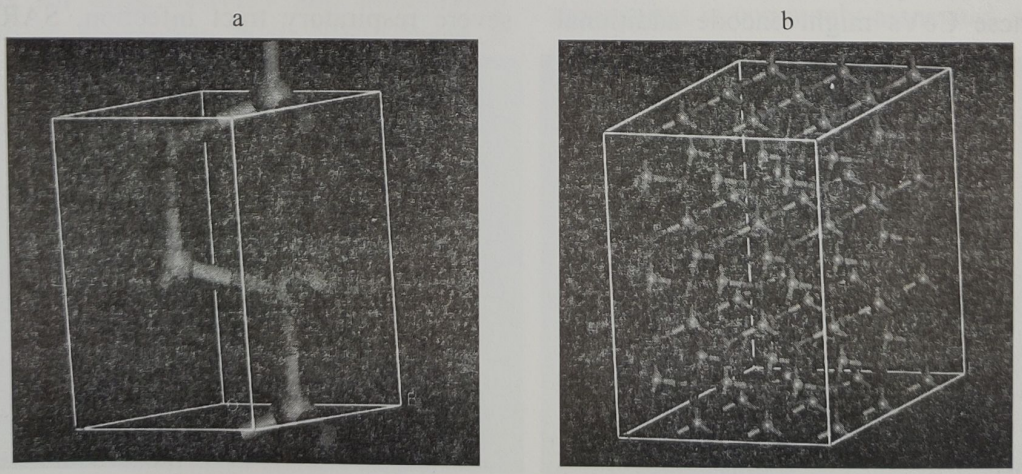

Fig. 2. *The geometry of ZnO (a) single cell, (b) super cell.*

The second component of this study is Alanine.

Alanine (abbreviations IUPAC-IUBMB: Ala or A) is an α-amino acid whose L-enantiomer is one of 22 proteinogenic amino acids, encoded on messenger RNAs by codons GCU, GCC, GCA and GCG. Alanine is an amino acid that goes into the composition of proteins.

It is characterized by an aliphatic apolar side chain. It is, along with serine, leucine and glycine, one of the most common amino acids in proteins.

The Alanine is in the lattice 3D Orthorhombic, and the crystallographic parameters for this single cell are $\alpha = 0.603$ nm, $b = 1.234$ nm, $c = 0.578$ nm and $\alpha = \beta = \gamma = 90°$.

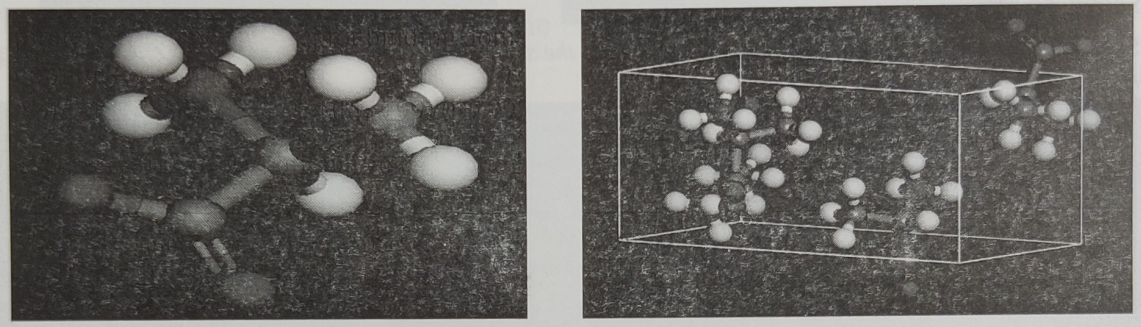

Fig. 3. *The geometry of Alanine molecule, single cell respectively.*

For the geometrical optimization of the two components ZnO and Alanine, we have made an insertion of the molecules of the Alanine cell in the super cell of ZnO.

Before starting the optimization, we calculated the distances between the atoms of Zn and the atoms of oxygen, and also the angles between them (Figs. 4, 5) super cell ZnO only, and (figs.6) super cell ZnO+Alanine.

NB. The measurements of the distances and angles before optimization are the same for the ZnO super cell with or without Alanine.

We notice that the distances between Zn and O before the optimization are identical and equal in the vertical direction of the super cell, and the atoms of Zn and O in the horizontal surface formed a very organized hexagonal structure and the distances and even the angles are identical (Figs. 4, 5, 6). The distances between Zn and O are identical and equal $D_{Zn\text{-}O}$vertical = 0.199nm and $D_{Zn\text{-}O}$ horizontal = 0.197nm.

The angles are also identical and equal, the angles in the vertical way = 108,044° and the angles in the horizontal way = 110,860°.

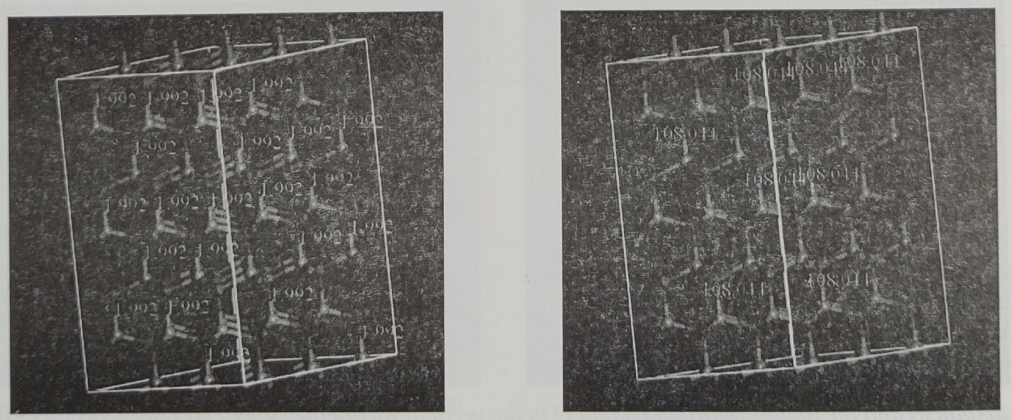

Fig. 4. *The distances and the angles between Zn and O in the vertical way of the super cell ZnO respectively.*

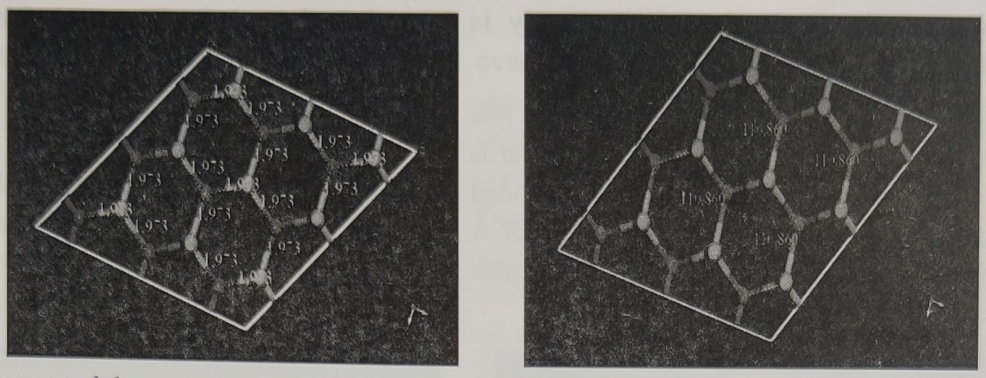

Fig. 5. *The distances and the angles between Zn and O in the surface horizontal of the supercell ZnO successively.*

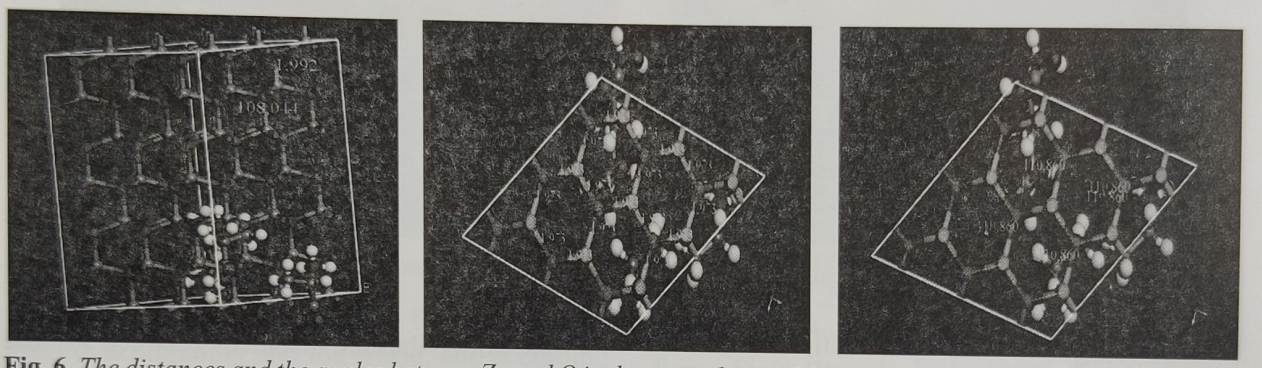

Fig. 6. *The distances and the angles between Zn and O in the vertical way of the super cell ZnO+Ala, the distances and the angles between Zn and O in the surface horizontal of the super cell of ZnO + Alanine respectively, before optimization. For all species, C = gray, H = white, O = red, Zn = mauve, N = blue.*

The ZnO building is well organized and well structured.

Results and Discussion

The results indicate that the distances and angles between atoms are completely changed; also the positions of Alanine molecules are changed in the super cell which means, there is a reaction between the atoms of ZnO and Alanine.

The results are illustrated in the following figures:

After the geometrical optimization the distances in the vertical direction are completely

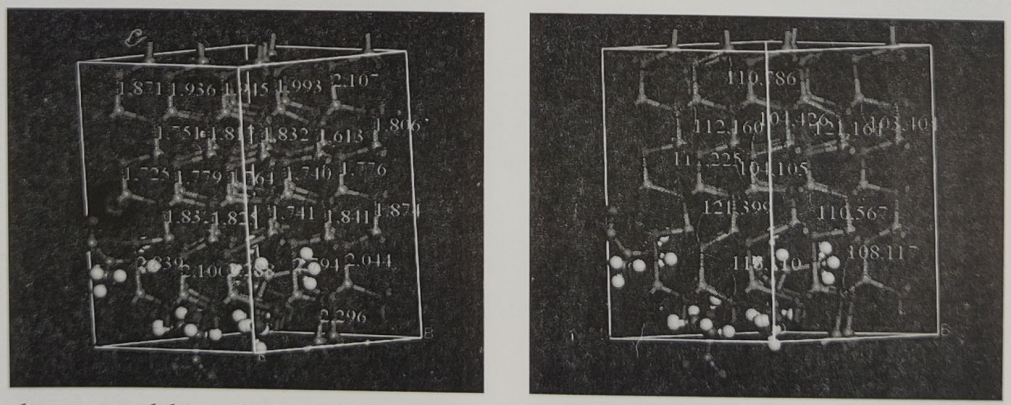

Fig. 7. *The distances and the angles between Zn and O in the vertical way of the super cell ZnO+Ala successively. After optimization. For all species, C = gray, H = white, O = red, Zn = mauve, N = blue.*

changed (distances are increased, and others are decreased), the angles also certain angles are decreased and others are increased.

The distances between Zn and O in the hexagonal surface are very changed and the well-organized hexagonal shape of ZnO is distorted, and the identical angles of the hexagonal shape are changed completely (Fig. 8).

The energy outcomes are shown in the (Table 1).

On the energetic side, the results given in the (Table 1), of super cell ZnO+Ala, indicate that enthalpy or total energy and also non-bonded energy and van der Waal's have large values before optimization compared to other energies, but after the optimization these previous energies are decreased, in the another hand the energies of bond, angle, torsion and inversion are very increased, because the bonds and angles are changed and the structure is deformed (Figs.7, 8), the bonds and the angles are in need of energies to make the deformation, this is why these energies are high.

Even the Alanine molecules are changed their positions in the ZnO super cell after the optimization which meant a reaction between ZnO and Alanine has happened, so this reaction influenced the whole ZnO super cell either in its structure or in energy rating according to the results obtained in this study.

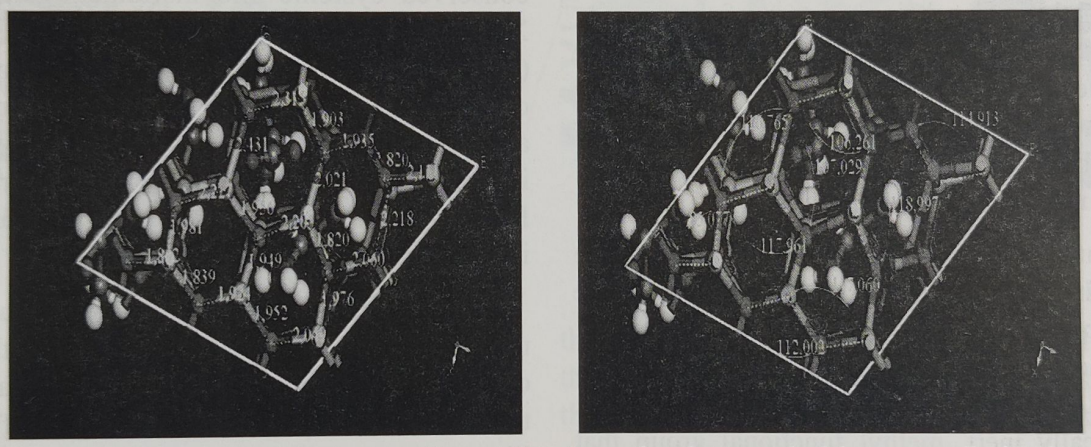

Fig. 8. *The distances and the angles between Zn and O in the surface horizontal of the super cell of ZnO + Alanine successively, after optimization. For all species, C = gray, H = white, O = red, Zn = mauve, N = blue.*

Table 1. *Energies before and after geometrical optimization of super cell ZnO+Ala.*

Energy (kcal mol|)	Super cell ZnO+Ala before optimization	Super cell ZnO+Ala after optimization
Total enthalpy	806644589.30	7292.20
Total energy	806644589.30	7292.20
Valence energy	1039.81	4676.45
Bond	919.97	3231.66
Angle	117.29	1302.82
Torsion	2.54	6.573
Inversion	0.001	135.39
Non-bonded energy	806643549.49	2615.74
van der Waals	806643553.08	2619.33
Electrostatic	0.00	0.00

As well, in the (Fig. 9) we observed that after optimization, the Zn molecules have disappeared from the structure of ZnO in the super cell, therefore the reaction of ZnO with Alanine deforms the structure of ZnO and cause ions of **Zn^{2+}** to be released.

In our study we chose Alanine because, it is one of the 20 amino acids mainly found in the peptide chains of proteins, and because of its exceptional properties where: Alanine (Ala) has propensity to form alpha helices but can also occur in beta sheets and is generally equivalent to simply truncating a side chain back to the beta carbon, which is the first side chain atom. The beta carbon position depends upon the back done dihedral angles of the polypeptide so is really part of the main chain structure of the protein. Thus, Alanine is generally an accepted single residue first choice for mutational scanning because it retains the beta carbon but no other side chain chemistry, and also known by their use in molecular biology scanning.

Further in molecular biology, **Alanine scanning** is a technique used to determine the contribution of a specific residue to the stability or function of given protein (Morrison, et al., 2001) Alanine is used because of its nonbulky, chemically inert, methyl functional group that nevertheless mimics the secondary structure preferences that many of the other amino acids possess. Sometimes bulky amino acids such as valine or leucine are used in cases where conservation of the size of mutated residues is needed. Alanine Scanning was used to determine simultaneously the functional contributions of 19 side chains buried at the interface between human growth hormone and the extracellular domain of its receptor (Weiss, *et al.,* 2000).

After the simulation and release of Zn^{2+} ions, and the existence of these ions in the protein environment, we talk about the zinc finger and its role with proteins. The abundance of Zn^{2+} ions in the medium of proteins leads to the abundance of proteins of Zinc fingers.

The zinc finger was first recognized 15 years ago as a repeated zinc-binding motif, containing conserved cysteine and histidine ligands, in Xenopus transcription factor IIIA (TFIIIA) (Miller, *et al.,* 1985). Since that time, numerous other zinc binding motifs have been identified and designated as zinc fingers. These vary widely in structure, as well as in function, which ranges from DNA or RNA binding to protein–protein interactions and membrane association.

A zinc finger is a small protein structural motif that is characterized by the coordination of one or more zinc ions (Zn^{2+}) in order to stabilize the fold. Originally coined to describe the finger-like appearance of a hypothesized structure from Xenopus laevis transcription factor IIIA, the zinc finger name has now come to encompass a wide variety of differing protein structures (Klug, *et*

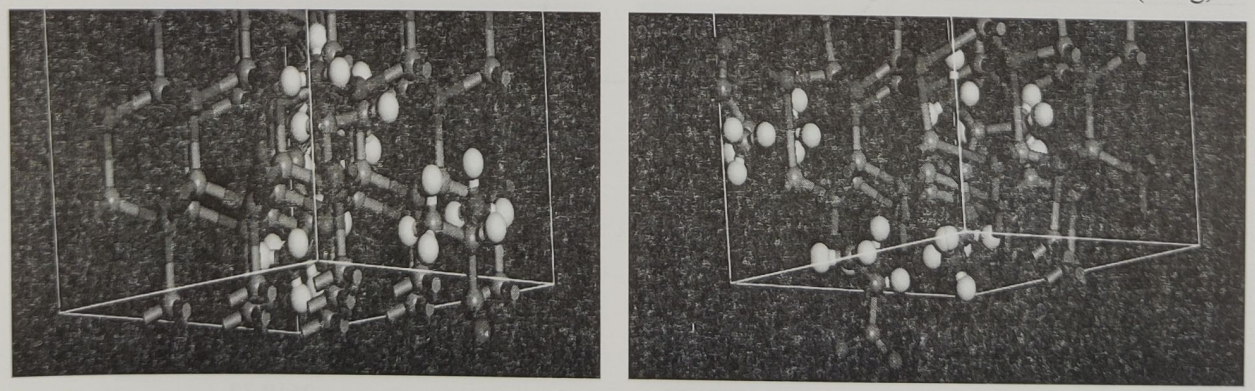

Fig. 9. *The position of the molecules of Alanine in the super cell ZnO before and after optimization successively. For all species, C = gray, H = white, O = red, Zn = mauve, N = blue.*

al., 1987). Xenopus laevis TFIIIA was originally demonstrated to contain zinc and require the metal for function in 1983, the first such reported zinc requirement for a gene regulatory protein (Hanas, *et al.*, 1983, Berg, 1990) It often appears as a metal binding domain in multi- domain proteins (Berg, 1990).

Zinc finger proteins are among the most abundant proteins in eukaryotic genomes. Their functions are extraordinarily diverse and include DNA recognition, RNA packaging, transcriptional activation, regulation of apoptosis, protein folding and assembly, and lipid binding. Zinc finger structures are as diverse as their functions.

Structure in 3D:

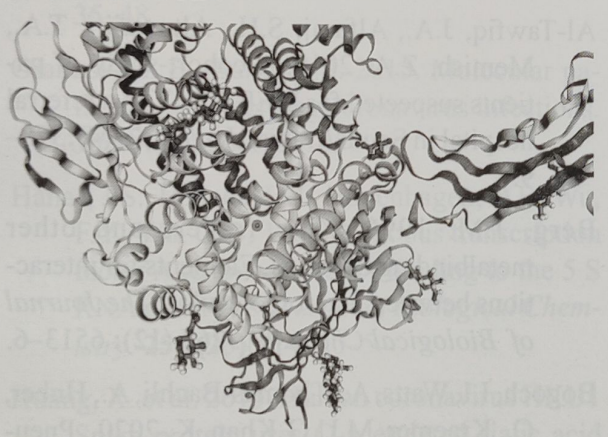

Fig. 10. *Structure in 3D of the coronavirus 229E with the protein and the ion of Zn^{2+} (in green sphere).*

Structures have recently been reported for many new zinc finger domains with novel topologies, providing important insights into structure/ function relationships. In addition, new structural studies of proteins containing the classical Cys2His2 zinc finger motif have led to novel insights into mechanisms of DNA binding and to a better understanding of their broader functions in transcriptional regulation. We take an example of CoV-229E coronavirus that infects humans, to see the interactions of Zn^{2+} with the molecules of the coronavirus and protein chains, according to the PDB (Protein Data Bank).

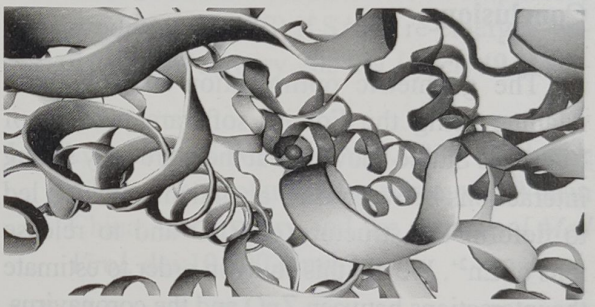

Fig. 11. Zoom on the Zn^{2+}.

As illustrated in the preceding figures from the PDB, Zn^{2+} in the reaction medium between the protein and the coronavirus, it interacts with the molecules of the chains, especially with the oxygen and nitrogen atoms.

Table 2. Data of the protein and the coronavirus 229E.

Molecule	Chains	Sequence Length	Organism	Gene Names
Aminopeptidase N	A, B	906	Homo sapiens	ANPEP (APN, CD13, PEPN)
Spike protein	C, D	145	Human coronavirus 229E	S

Table 3. *Data of the ligand Zn^{2+}*

Ligands (ID)	Chains	Name / Formula / InChI Key	2D Diagram & Interactions
Zn	A, B	**ZINC ION** Zn PTFCDOFLOPIGGS-UHFFFAOYSA-N	**Zn^{2+}**

Ligand Interaction

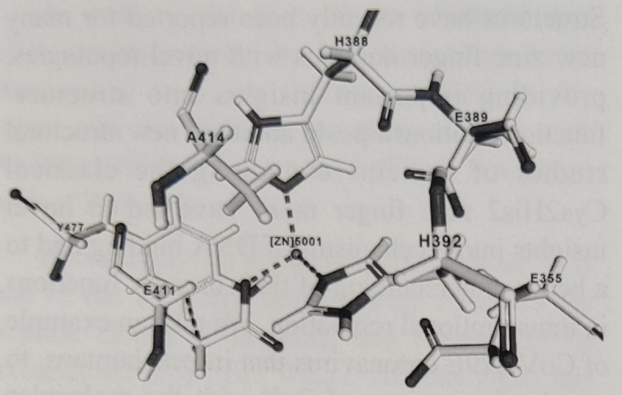

Fig. 12. The interaction of the ligand Zn^{2+} with the molecule of the protein and the coronavirus 229E.

Conclusion

The geometric optimization of ZnO with Alanine using the Forcite software module of Materials Studio showed that there are very strong interactions between ZnO and Alanine which led to deform the structure of ZnO and to release ions of Zn^{2+}. We did this study in order to estimate the interactions between ZnO and the coronavirus, hoping to find a solution for this deadly virus. In fact this study showed us that it has a chance. The release of Zn^{2+} in the protein environment allows us to talk about the proteins of Zinc fingers, the latter their functions are extraordinarily diverse and include recognition of DNA, conditioning of RNA, transcriptional activation, the regulation of apoptosis, the folding and assembly of proteins and lipid binding. The structures of zinc fingers are as diverse as their functions. Structures have recently been reported for many new zinc finger domains with new topologies, providing important information on structure / function relationships. In addition, new structural studies of proteins containing the classical zinc finger motif Cys2His2 have led to new insights into DNA binding mechanisms and a better understanding of their broader functions in transcriptional regulation, therefore the abundance of Zn^{2+} in the medium of proteins to the abundance of proteins of the Zinc fingers. It can help influence the coronavirus and its structure.

References

Accelrys Software Inc. 2012: Forcite program. *San Diego, CA.*

Alonso, S., Izeta, A., Sola, L and Enjuanes, L. 2002a. Transcription regulatory sequences and mRNA expression levels in the coronavirus transmissible gastroenteritis virus. *J. Viral.* **76:** 1293-1308.

Alonso, S., Sola, L., Teifke, J., Reimann, L., Izeta, A., Balach, M., Plana-Duran, J., Moormann, R. J. M. and Enjuanes, L. 2002b. In vitro and in vivo expression of foreign genes by transmissible gastroenteritis coronavirus-derived minigenomes. *J. Gen. Viral.* **83:** 000-000.

Al-Tawfiq, J.A., Alfaraj, S.H., Altuwaijri, T.A., Memish, Z.A. 2017. A cohort-study of patients suspected for MERS-CoV in a referral hospital in Saudi Arabia. *J Infect.* **75(4):**378–9.

Berg, J.M. 1990. Zinc fingers and other metalbinding domains. Elements for interactions between macromolecules. *The Journal of Biological Chemistry.* **265 (12):** 6513–6.

Bogoch, I.I, Watts, A., Thomas-Bachli, A., Huber, C., Kraemer, M.U.G, Khan, K. 2020. Pneumonia of unknown etiology in Wuhan, China: potential for international spread via commercial air travel. *J Travel Med.* doi:10.1093/jtm/taaa008

Butler, N., et al. 2006. Murine encephalitis caused by HCoV-OC43, a human coronavirus with broad species specificity, is partly immune-mediated. *Virology.* **347:** 410–421

DeDiego, M.L., Álvarez, E., Almazán, F., Rejas, M.T., Lamirande, E., Roberts, A., et al. 2007. A severe acute respiratory syndrome coronavirus that lacks the E gene is attenuated *in vitro* and *in vivo*. *J Virol.* **81(4) :** 1701–13.

De Groot, R.J. 2011. Family Coronaviridae. In Ninth Report of the International Commit-

tee on Taxonomy of Viruses (King, A.M.Q. et al. eds). *Elsevier, Oxford*. 806–828.

Escors, D., Ortego, J., Laude, H. and Enjuanes, L. 2001a. The membrane M protein carboxy terminus binds to transmissible gastroenteritis coronavirus core and contributes to core stability. *J. Viral.* **75 :** 1312-1324.

Escors, D., Ortego, J., Laude, H. and Enjuanes, L. 2001b. Organization of two transmissible gastroenteritis coronavirus membrane protein topologies within the virion and core. *J. Viral.* **75:** 12228- 12240.

Forni, D., Cargliani, R., Clerici, M., Sironi, M. 2017. Molecular evolution of human coronavirus genomes. *Trends Microbiol.* **25:** 35–48.

Gralinski, L.E., Baric, R.S. 2015. Molecular pathology of emerging coronavirus infections. *J Pathol.* **235:**185-195.

Hanas, J.S., Hazuda, D.J., Bogenhagen, D.F., Wu, F.Y., Wu, C.W. 1983. Xenopus transcription factor A requires zinc for binding to the 5 S RNA gene. *The Journal of Biological Chemistry*. **258 (23) :** 14120–5.

Huang, X. et al. 2015. Human coronavirus HKU1 Spike protein uses O-acetylated sialic acid as an attachment receptor determinant and employs hemagglutininesterase protein as a receptor-destroying enzyme. *J. Virol.* **89:**7202–7213.

Jiang, J., Pi, J. and Cai, J. 2018. The Advancing of Zinc Oxide Nanoparticles for Biomedical Applications, *Bioinorganic Chemistry and Applications*. **(3):** 1-18

Kim, S., Lee, S. Y. and Cho, H. J. 2017. Doxorubicin-wrapped zinc oxide nanoclusters for the therapy of colorectal adenocarcinoma. *Nanomaterials.* **7(11):** 354.

Klug, A., Rhodes, D. 1987. Zinc fingers: a novel protein fold for nucleic acid recognition. *Cold Spring Harbor Symposia on Quantitative Biology*. **52:** 473– 82.

Kuo, L., Masters, P.S. 2003. The small envelope protein E is not essential for murine coronavirus replication. *J Virol.* **77(8):**4597–608.

Li, W., et al. 2003 .Angiotensin-converting enzyme 2 is a functional receptor for the SARS coronavirus. *Nature.* **426:**450–454

Lim, W.S., Anderson, S.R., Read, R.C. 2004. SARS Guidelines Committee of the British Thoracic Society; British Infection Society; Health Protection Agency. Hospital management of adults with severe acute respiratory syndrome (SARS) if SARS re-emerges–updated 10 February 2004. *J Infect.* **49 (1):**1–7.

Lu, H., Stratton, C.W., Tang, Y.W. 2020. Outbreak of pneumonia of unknown etiology in Wuhan China: the mystery and the miracle. *J Med Virol*. doi:10.1002/jmv.25678.

Luk, H.K.H., Li, X., Fung, J., Lau, S.K.P., Woo, P.C.Y., 2019. Mol ecular epidemiology, evolution and phylogeny of SARS coronavirus. *Infect. Genet. Evol.* 21-30.

Masters, P.S. 2006. The molecular biology of coronaviruses. *Adv Virus Res.* **66:** 193–292.

Masters, P.S., Perlman, S. 2013. Coronaviridae. *In Field's Virology,* edn 6th. Edited by Knipe, Howley. Wolters Kluwer/Lippincott Williams *& Wilkins Health.* **:** 825-858.

Materials Studio. Accelrys Software Inc., San Diego. Note that some of these codes were also offered as part of the Cerius 2 application that preceded Materials Studio; 2013. Available from http://accelrys.com/products/materials-studio/

Miller, J., McLachlan, A.D., Klug, A. 1985. Repetitive zinc-binding domains in the protein transcription factor IIIA from Xenopus oocytes. EMBO J. **4:** 1609-1614.

Mishra, P. K., Mishra, H., Ekielski, A.,

Talegaonkar, S. and Vaidya, B. 2017. Zinc oxide nanoparticles: a promising nanomaterial for biomedical applications. *Drug Discovery Today*. **22 (12) :** 1825-1834.

Morrison, K.L., Weiss, G.A. 2001. Combinatorial alanine-scanning. *Curr Opin Chem Biol.* **5 (3):** 302–7.

Mortola, E., Roy, P. 2004. Efficient assembly and release of SARS coronavirus-like particles by a heterologous expression system. *FEBS Lett.* **576(1–2):**174–8.

Ortego, J., Ceriani, J.E., Patiño, C., Plana, J., Enjuanes, L. 2007. Absence of E protein arrests transmissible gastroenteritis coronavirus maturation in the secretory pathway. *Virology.* **368(2) :** 296–308.

Padmavathy, N., Vijayaraghavan, R. 2008. Enhanced bioactivity of ZnO nanoparticles- an antimicrobial study. *Sci Technol Adv Mater.* **9:** 1-7.

Piccinno, F., Gottschalk, F., Seeger, S., Nowack, B. 2012. Industrial production quantities and uses of ten engineered nanomaterials for Europe and the world. *J Nanopart Res.* **14:** 1109-20.

Ramadan, N., Shaib, H. 2019. Middle East respiratory syndrome coronavirus (MERSCoV): *A review. Germs.* **9:** 35–42.

Rappé, A.K., Casewit, C.J., Colwell, K.S., Goddard III, W.A. and Skiff, W.M. Uff.1992. A full periodic table force field for molecular mechanics and molecular dynamics simulation. *J. Amer. Chemical Soc.* **114** (25) : 10024-10035.

Rasmussen, J.W., Martinez, E., Louka, P., and Wingett, D. G. 2010. Zinc oxide nanoparticles for selective destruction of tumor cells and potential for drug delivery applications, *Expert Opinion on Drug Delivery.* **7(9) :** 1063–1077.

Reinier L.C. Akkermans, Neil A. Spenley and Struan H. Robertson, 2015. Monte Carlo methods in Materials Studio. *Molecular Simulation.* **39**(14-15): 1153-1164.

Ruch, T.R., Machamer, C.E. 2012. The coronavirus E protein: Assembly and beyond. *Viruses.* **4(3)** : 363–82.

Sarivastava, R. 2012. Synthesis and Characterization Techniques of Nanomaterials. *International Journal of Green Nanotechnology.* **4:** 17-27.

Siu, Y., Teoh, K., Lo, J., Chan, C., Kien, F., Escriou, N., et al. 2008. The M, E, and N structural proteins of the severe acute respiratory syndrome coronavirus are required for efficient assembly, trafficking, and release of virus-like particles. *J Virol.* **82 (22) :** 11318–30.

Su, S., Wong, G., Shi, W., Liu, J., Lai, A.C.K., Zhou, J., Liu, W., Bi, Y., Gao, G.F. 2016. Epidemiology, genetic recombination, and pathogenesis of coronaviruses. *Trends Microbiol.* **24:** 490–502.

Swain, P. S., Rao, S. B.N., Rajendran, D., Dominic, G., Selvaraju, S. 2016. Nano zinc, an alternative to conventional zinc as animal feed supplement: A review Animal Nutrition **2:** 134-141.

van Doremalen, N., et al. 2014. Host species restriction of Middle East respiratory syndrome coronavirus through its receptor, dipeptidyl peptidase. *J. Virol.* **88:** 9220–9232.

Wang, C., Zheng, X., Gai, W., Zhao, Y., Wang, H., Wang, H., et al. 2017. MERS-CoV virus-like particles produced in insect cells induce specific humoural and cellular immunity in rhesus macaques. *Oncotarget.* **8(8) :** 12686–94.

Weiss, G.A., Watanabe, C.K., Zhong, A., Goddard, A., Sidhu, S.S. 2000. Rapid mapping of protein functional epitopes by combinatorial alanine scanning. *Proc. Natl. Acad. Sci. U.S.A.* **97 (16):** 8950–4.

Woo, P.C. *et al.* 2012. Discovery of seven novel mammalian and avian coronaviruses in the genus deltacoronavirus supports bat coronaviruses as the gene source of alphacoronavirus and betacoronavirus and avian coronaviruses as the gene source of gammacoronavirus and deltacoronavirus. *J. Virol.* **86:** 3995-4008.

Wu, K., et al. 2009. Crystal structure of NL63 respiratory coronavirus receptor binding domain complexed with its human receptor. *Proc. Natl. Acad. Sci. U. S. A.* **106:** 19970–19974

Xiong, H. M. 2013. ZnO nanoparticles applied to bioimaging and drug delivery, *Advanced Materials.* 25(37): 5329–5335.

Yeager, C.L., et al. 1992. Human aminopeptidase N is a receptor for human coronavirus 229E. *Nature.* **357:** 420–422.

Zhang, Y., Nayak, T. R., Hong, H., and Cai, W. 2013. Biomedical applications of zinc oxide nanomaterials. *Current molecular medicine*, **13(10):** 1633-1645.

Zhang, Z. Y. and Xiong, H. M. 2015. Photoluminescent ZnO nanoparticles and their biological applications. *Materials.* **8(6):** 3101–3127.

(Commissioned: 14 February 2020; Received: 01 March 2020; Accepted: 20 April 2020)

Clay Research, Vol. 38, No. 2, pp. 56-62 (2019)

Clay Mineralogical and Geochemical Evidences of Lateritic Weathering at about 2.2 Ga prior to the Evolution of Life on Earth

ROHIT KUMAR [a], NANDAN KUMAR [b] AND PANKAJ SRIVASTAVA [c,*]

[a] *Department of Geology, University of Delhi, Delhi*
[b] *Geological Survey of India, Western Region, Jaipur*

Abstract *– This study incorporates a well-developed lateritic profile occurring within the Aravalli Supergroup sediments of 2200 Ma-1850 Ma age from Rajasthan, Western India. The lateritic paleosol exposed in a 60 m query was studied for field characteristics, clay mineralogy, and geochemical features to assess weathering and paleoclimatic conditions during Precambrian. The paleosol is marked by intense weathering with deep-red and light orange colours, massive to friable blocky structure, which progressively grades down to unaltered dolomite in the lower most part. The X-ray diffraction studies of the total clay (<2 μm) and the fine clay (<0.2 μm) fractions of the lateritic paleosols are characterized by 7A°, 3.58 A°, 3.52 A°, and 3.03A° mineral assemblage dominated by the kaolinite and anatase in large amounts. Other clay minerals include halloysite, mixed layers of kaolinite-halloysite, and calcite-veterite in small proportions. The energy dispersive X-Ray spectrometry (EDS) analysis of a few concretions show large scale enrichment of Al, Fe and Ti and the losses of the Ca, Mg, Na, and K during weathering and formation of the clay minerals. These features provide the evidence of intense weathering conditions under hot-humid climate leading to the formation of laterite prior to evolution of life on Earth at about 2.2 Ga.*

Keywords: Aravallies, Evolution of life, Laterization, Precambrian, Weathering.

The term "laterite" was first described by Francis Buchman (1807) as a hard iron rich material cut for building in western peninsular India. Over the last 200 years this term has become a topic of intense research and debate (Schellmann, 1986; Pendleton, 1936; Kellogg, 1949; Nahon and Tardy, 1992). This was described as an intense subaerial weathering product whose Fe and/or Al content is higher and Si content is lower than in the parent rocks (Schellmann, 1986). Others have described the laterite as the product of intense weathering made up of mineral assemblages that may include iron or aluminium oxides, oxyhydroxides or hydroxides, kaolinite and quartz, generally forming under tropical conditions (Pendleton, 1936; Kellogg, 1949; Nahon and Tardy, 1992). In general, a lateritic profile is characterized by a massive, blocky, vesicular, cellular, concretionary and/or conglomerate zone overlying a mottled zone, pallid zone and weathered zone dominated by a large and variable proportions of iron and alumina oxides (Schellmann, 1986; Pendleton, 1936; Kellogg, 1949; Nahon and Tardy, 1992).

In the modern tropical condition, the laterites can form through direct weathering of feldspar (Anand *et al.,* 1985) or by neosynthesis as a product of hydrolysis (De Kimpe *et al.,* 1961; Rengasamy *et al.,* 1978) or by the intermediate mica stage (Gilkes and Suddhiprakarn, 1979). The X-Ray diffraction (XRD) analysis of the modern tropical laterites suggest it is dominated

***Corresponding Author's email:** pankajps@gmail.com
DOI: 10.5958/0974-4509.2019.00002.0

by the kaolinite mineralogy (Chandran *et al.,* 2005). If the kaolinite is derived from the basaltic soils, mostly it is poorly ordered structure, and if it from the granite and sedimentary rock, it shows ordered structure (Hart *et al.,* 2002). In term of environment, hydrating environment are favourable for the formation of poorly ordered kaolinite (McFarlane, 1976) and if the elevation and precipitation increases, a gradual dominance of well-ordered kaolinite has been reported from an altitudinal sequence (Darwish and Zurayk, 1997). Crystallinity of kaolinite generally decreases as length of the dry season decreases (Hughes and Brown, 1979). It was reported that planner kaolinite transforms to tabular halloysite by hydration and exfoliation in wet paleoenvironments (Singh, 1996).

Precambrian laterite or paleosols are considered as one of the most important sources of information about the oxygenation in Earth's early atmosphere and the oxidation state of the Precambrian environment in which they formed. (Holland, 1984; Retallack,1984; Furian et al., 2002). This is based on the analogy that weathering is the near surface process and occurs in contact with hydrosphere, atmosphere and lithosphere in the past as well as in recent times (Wilding and Lin, 2006). Therefore, clay mineralogy and geochemistry of the paleosols reflect the nature of the atmosphere at the time of weathering and pedogenesis. Precambrian laterites/paleosol has been reported by various workers all around the globe (Reimer,1986; Gutzmer and Beukes,1998; Furian *et al.,* 2002; Beukes *et al.,* 2002; Crowe *et al.,* 2013). Some of the workers have shown the evidences of the earliest signature of biomass similar to modern tropical environments in the pallid zone of the lateritic profiles (Gutzmer and Beukes,1998; Beukes *et al.,* 2002). The widespread occurrence of the laterite in the southern and the central India range in age from late Cretaceous to early Tertiary on the basis of magnetic and paleolatitudinal studies (Schimdt *et al.,* 1983; Kumar, 1986).

Despite the fact that Indian Plate has remained an integral part of the all major geological events throughout the geological history since its origin, which must include the laterization and weathering processes during Precambrian time. However, there are no reports of the Precambrian laterite occurring in India. This study reports the lateritic weathering within the Aravalli Supergroup which is the direct product of the early Proterozoic weathering at about 2.2 Ga. X-ray diffraction analysis of the clay minerals and the geochemical characters based on EDS analysis of different horizons of the lateritic profile from Aravalli Supergroup of sediments has been carried out to understand the weathering characteristics, paleoenvironments and pedogenesis during the formation of the laterite in the Precambrian time.

Geological Settings

The Aravalli Supergroup (AS) of sediments overlies basement i.e. is deposited over the Banded Gneissic Complex (BGC) with an erosional unconformity (Fig. 1). The AS is characterized by a thick pile of less metamorphosed but complexly folded Paleoproterozoic sediments and basic volcanics. Traditionally this is subdivided as Lower, Middle and Upper Aravalli Groups (Heron, 1953; Roy,

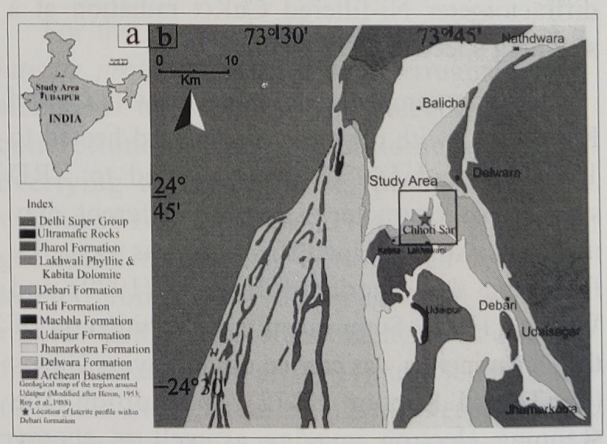

Fig. 1. *(a) Location of study area in India, (b) General geological map of the Aravalli Supergroup and the location of the lateritic profile within Debari Formation (marked as *) (after Heron, 1953; Roy et al.,1988).*

1988). This study is related to Debari Formation occurring within the Middle Aravalli Group of sediments. The Debari Formation lithology is mainly defined by the quartzite, the phyllite and the carbonate facies, which correspond to near shore shelf sedimentary environment (Sinha-Roy *et al.,* 1993b). This study is related to a ~15 meter thick deep red, orange and ochre lateritic profile occurring within Debari Formation near Sar Village, Udaipur, Rajasthan.

Materials and Methods

In the Present study, the ~15 m lateritic profile was subsampled horizon wise for clay mineralogy and geochemical analysis. The particle size fractionation was carried out following the guideline by Jackson (1979). Accordingly, air-dried samples containing no particle larger than 2 mm were treated for removal of excess salts and $CaCO_3$ by Sodium Acetate and further with Sodium Citrate Dihydrate, Sodium Bicarbonate and Sodium Dithionite to removal of free iron oxides. The silt (50-2 μm), total clay (<2 μm) and fine clay (<0.2 μm) fractions were fractionated following the size segregation procedure (Jackson, 1979). The oriented total and fine clay fractions were subjected to X-ray diffraction (XRD) analysis using a Philips diffractometer Ni-filtered CuKα radiation at a scanning speed of 2°2θ/min.

The clay samples were saturated with Ca and K, solvated with ethylene glycol, and heated to 110, 300, and 550°C and subjected to XRD studies for characterization of different clay minerals. Mineral identification was done by following the criteria of Jackson (1979) and Wilson (1987). Semi-quantitative estimation of the clay minerals was carried out following Gjems (1967) and Kapoor (1972). In addition, the scanning electron imaging as well as energy dispersive X-Ray spectrometry (EDS) were applied to thin section of the samples to obtain mineralogical and chemical data of the samples using a Scanning electron microscopy (JCM-6000 Plus Versatile Benchtop SEM) equipped with an energy dispersive X-Ray spectrometer at Delhi University.

Results

Macromorphological features of the Precambrian Laterite

The ~15 m profile is characterized by colour variation from very light orange colour to deep red colour (10R), pisolitic concretions and nodules of 4-5 mm to 20-30 mm size and concentric features (Fig. 2). The horizons show excessive mottling and vary from soft to very hard in nature. These paleosols are also marked by massive to blocky structure.

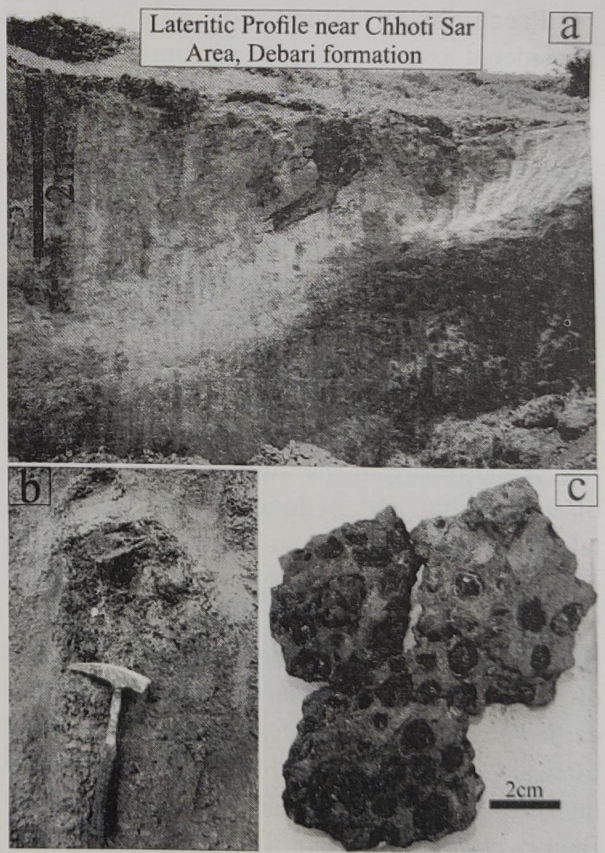

Fig. 2. (a) ***Outcrop of the*** *Precambrian laterite Debari Formation,* **(b)** *Enlarged view of the lateritic profile showing the zone of pisolitic concretions,* **(c)** *Hand specimens of the laterite showing rounded to sub-rounded deep red colour concretions and nodules.*

Clay mineralogy of the Precambrian laterites

The X-Ray diffraction pattern (XRD) of the total clay fractions (<2 ìm) show strong and sharp peaks for 0.71 nm, 0.358 nm, 0.352 nm and 0.303 nm minerals (Fig.3a). On glycolation there is a slight broadening of the 0.71 nm peak and in K-saturated and heating from 110° C to 550° C, the intensity of the peak 0.71 nm is almost similar till 330° C, which collapses at 550° C (Fig. 3a). The XRD features of the fine clay fraction (<0.2 ìm) are similar to the total clay fraction with (Fig. 3b). The total and fine clay fraction corresponds to dominance of kaolinite and anatase in large amounts. Other clay minerals include halloysite, mixed layers of kaolinite-halloysite, and calcite-veterite in small proportions (Fig. 3 a, b).

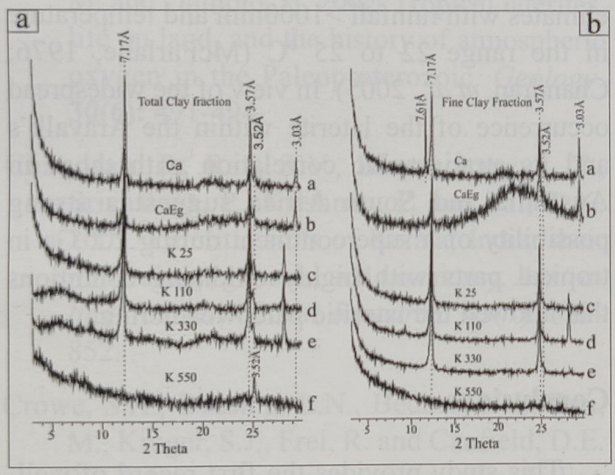

Fig. 3. (a) *XRD of total clay,* **(b)** *XRD of the fine clay of the laterite (a: Ca saturated, b: Ca saturated and glycolated, c: K saturated at 25°C, d: K saturated and heated to 110°C, e: K saturated and heated to 330°C, f: K saturated and heated to 550°C).*

Energy Dispersive X-Ray (EDS) spectrum of the pisolitic nodules

Energy Dispersive X-Ray (EDS) spectrum which was carried out for a few critical pisolitic concretions for the light buff white point and dark red to orange parts are characterized by several peaks corresponding to 0.5 KeV,1.4 KeV,1.7 KeV, 4.5 KeV, 5.8 KeV and 6.3 KeV (Figs. 2 a-d). These peaks correspond to Ti, Fe, Al, Si, Mn elements in large amount and minor concentration of Mg, Na, Ca elements (Figs. 4 a-d). The dark red to orange concentric layers is characterized by the dominance of SiO_2 (42.5%), Al_2O_3 (35.6%), FeO (17.5%) and others including Na_2O, MgO, K_2O, CaO, and MnO in <1% (Figs. 4 a, c). Whereas, the light buff white concentric layers are characterized by the dominance of TiO_2 (60.7%), and FeO (37.5%), while others including SiO_2, Al_2O_3, Na_2O, MgO, K_2O, CaO, and MnO occur in minor amounts as <1% (Figs. 4 b, d).

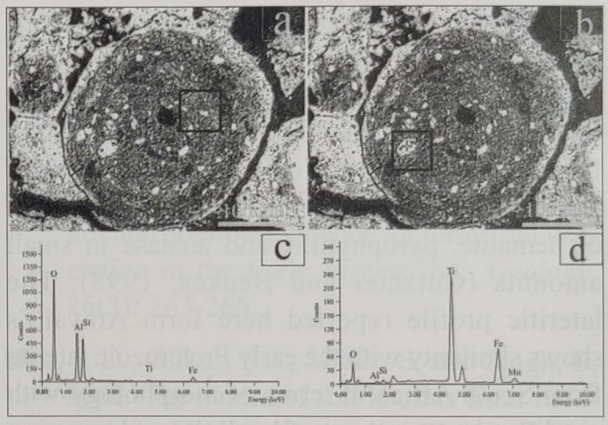

Fig. 4. *EDS analysis for the dark red to orange parts* **(a)** *and light buff white* point **(b)** *and corresponding peaks in* **(c)** *for the dark red to orange part and in* **(d)** *for light buff white point.*

Discussion

For the purpose of discussion, in general a *laterite profile* is defined as a ferruginous and aluminous massive, blocky, vesicular, cellular, concretionary and or conglomeratic zone overlying a mottled zone, pallid zone and weathered zone (Firman, 1994). The ages of the geological record that contain well-developed lateritic profiles show varying ages with the oldest records from Precambrian Shields such as those from Australia (Firman, 1994) and South Africa (Gutzmer and Beukes, 1998; Beukes *et al.,* 2002). These profiles define the oldest weathering record of the Earth which occur as sporadically within the modern regolith on account of subsequent erosions and the evolution of newer profile

(Gutzmer and Beukes, 1998; Beukes *et al.,* 2002). However, this study provides the first evidence of well-preserved lateritic profile within Paleoproterozoic sediments of 2.2 Ga age from India. The reported lateritic paleosol is underlain and overlain by shallow marine sediments. This suggest uplift and resurrection of the marginal parts of the Aravalli Carton for prolonged duration and subaerial weathering leading to the formation of lateritic profiles within the Debari Formation of the Aravalli super group.

The clay mineralogy of the Precambrian laterites reported from Australia and South Africa show extensive kaolinization of the parent material under extreme weathering conditions (Gutzmer and Beukes, 1998; Beukes *et al.,* 2002). In addition to the kaolinite, the laterites from South Africa show pisoliths with large amount of hematite, pyrophyllite, and anatase in small amounts (Gutzmer and Beukes, 1998). The lateritic profile reported here form Aravalli's shows similarity with the early Proterozoic laterite from South Africa in terms of morphology with pisoliths, large amount of kaolinite and presence of anatase. This kind of clay mineral assemblage suggests diagenetic or metamorphic alteration of a kaolinite rich material with variable amount of Al-, Fe-, and Ti-oxides, which defines the modern laterite (Bárdossy and Aleva, 1990).

The geochemical characters of the pisoliths based on EDS analysis show that light or buff white layers show enrichment of TiO_2 (60.7%), and FeO (37.5%), but depletion of SiO_2, Al_2O_3, Na_2O, MgO, K_2O, CaO, and MnO (<1%). This pattern of depletion is comparable to the bleached zone of the modern laterite (McFarlane, 1976). Whereas, the dark red layers are enriched in SiO_2 (42.5%), Al_2O_3 (35.6%), FeO (17.5%) and large depletion of Na_2O, MgO, K_2O, CaO, and MnO (<1%). This is also in confirmation of the deep red iron and alumina rich parts of the modern laterite (McFarlane, 1976). Both the light and dark layers of the pisoliths show very low concentration the Na, K, Ca, Mg elements and suggest extreme leaching and intense weathering and laterization (Maynard, 1992).

The Paleoproterozoic lateritic profile reported here from Aravalli Supergroup is very significant for the paleoenvironments information of the early life, oxygenation and evolution of the Earth. The lateritic profile reported here shows its widespread occurrence in several other parts in similar stratigraphic settings, which indicates a mature landscape that was conducive for the early Proterozoic laterization in the Aravallies. The occurrence of the laterite in different continents e.g. Australia, South Africa, and India suggest widespread and global scale laterization at 2.0 to 2.2 Ga.

The modern laterite formation normally occurs in warm humid tropical to subtropical climates with rainfall >1000mm and temperature in the range 22 to 25 °C (McFarlane, 1976; Chandran, *et al.,* 2005). In view of the widespread occurrence of the laterite within the Aravalli's and its stratigraphic correlation with those in Australia and South Africa suggest a strong possibility of a supercontinent during 2.2 Ga in tropical parts with highly oxidising conditions that allowed the lateritic paleoweathering.

Conclusions

This study provides the first record of well-preserved lateritic profile within Paleoproterozoic sediments of 2.2 Ga age from Aravalli Supergroup. This indicates prolonged subaerial weathering in tropical to subtropical conditions and the formation of lateritic profiles within the AS.

The pisoliths with alternate light and dark concentric layers, clay mineral assemblage dominated by the kaolinite and small amounts of Anatase, enrichment of Al_2O_3, Fe_2O_3, and TiO_2 and extensive depletion of Na, K, Ca, and Mg suggest extreme weathering conditions similar to those in modern laterites.

The widespread occurrence the Paleoproterozoic laterite in Aravallies and its stratigraphic correlation with those in Australia and South Africa suggests global scale laterization under tropical conditions and highly oxidizing atmosphere at about 2.2 Ga.

References

Anand, R.R., Gilkes, R.J., Armitage, T.M. and Hillyer, J.W. 1985. Feldspar weathering in lateritic saprolite. *Clays and Clay Minerals.* **33**(1): 31-43.

Bárdossy, G. and Aleva, G.J.J. 1990. *Lateritic bauxites* (Vol. 27). Elsevier, Amsterdam.

Beukes, N.J., Dorland, H., Gutzmer, J., Nedachi, M. and Ohmoto, H. 2002. Tropical laterites, life on land, and the history of atmospheric oxygen in the Paleoproterozoic. *Geology.* **30(6):** 491-494.

Chandran, P., Ray, S.V., Bhattacharyya, T., Srivastava, P., Krishnan, P. and Pal, D.K. 2005. Lateritic soils of Kerala, India: their mineralogy, genesis, and taxonomy. *Australian Journal of Soil Research.* **43**(7): 839-852.

Crowe, S.A., Døssing, L.N., Beukes, N.J., Bau, M., Kruger, S.J., Frei, R. and Canfield, D.E. 2013. Atmospheric oxygenation three billion years ago. *Nature.* **501**(7468): 535.

Darwish, T.M. and Zurayk, R.A. 1997. Distribution and nature of Red Mediterranean soils in Lebanon along an altitudinal sequence. *Catena.* **28(3-4):** 191-202.

De Kimpe, C., Gastuche, M.C. and Brindley, G.W. 1961. Ionic coordination in alumino-silicic gels in relation to clay mineral formation. *American Mineralogist: Journal of Earth and Planetary Materials.* **46(11-12):** 1370-1381.

Firman, J.B. 1994. Paleosols in laterite and silcrete profiles Evidence from the South East Margin of the Australian Precambrian Shield. *Earth-Science Reviews.* **36(3-4):** 149-179.

Furian, S., Barbiero, L., Boulet, R., Curmi, P., Grimaldi, M. and Grimaldi, C. 2002. Distribution and dynamics of gibbsite and kaolinite in an oxisol of Serra do Mar, southeastern Brazil. *Geoderma.* **106(1-2):** 83-100.

Gilkes, R.J. and Suddhiprakarn, A. 1979. Biotite alteration in deeply weathered granite. I. Morphological, mineralogical, and chemical properties. *Clays and Clay Minerals.* **27(5):** 349-360.

Gjems, O. 1967. Studies on clay minerals and clay-mineral formation in soil profiles in Scandinavia. *Med. Nor. Skogforksvesen.* **21:** 303-415.

Gutzmer, J. and Beukes, N.J. 1998. Earliest laterites and possible evidence for terrestrial vegetation in the Early Proterozoic. *Geology.* **26(3):** 263-266.

Hart, R.D., Gilkes, R.J., Siradz, S. and Singh, B. 2002. The nature of soil kaolins from Indonesia and Western Australia. *Clays and Clay Minerals.* **50(2):** 198-207.

Heron, A.M. 1953. The geology of central Rajputana. *Mem. Geol. Soc. Ind., 79.*

Holland, H.D. 1984. *The chemical evolution of the atmosphere and oceans.* Princeton University Press. 598 pp.

Hughes, J.C. and Brown, G. 1979. A crystallinity index for soil kaolins and its relation to parent rock, climate and soil maturity. *J. Soil Sci.* **30**(3): 557-563.

Jackson, M.L. 1979. *Soil Chemical Analysis– Advanced Course.* 2nd edn., Published by the author, University of Wisconsin, Madison.

Kapoor, B.S. 1972. Weathering of micaceous clays in some Norwegian podzols. *Clay Minerals.* **9(4):** 383-394.

Kellogg, C.E. 1949. Preliminary suggestions for the classification and nomenclature of great

soil groups in tropical and equatorial regions. *Commonwealth Bureau of Soil Science Technical Communication*. **46:** 76-85.

Kumar, A. 1986. Palaeolatitudes and the age of Indian laterites. *Palaeogeography, Palaeoclimatology, Palaeoecology*. **53(2-4):** 231-237.

Maynard, J.B. 1992. Chemistry of modern soils as a guide to interpreting Precambrian paleosols. *The Journal of Geology*. **100(3):** 279-289.

McFarlane, M.J. 1976. *Laterite and landscape*. Academic Press. 164 pp.

Nahon, D. and Tardy, Y. 1992. The ferruginous laterites. In *Handbook of exploration geochemistry,* Elsevier, Vol. 4, pp.41-55.

Pendleton, R.L. 1936. On the use of the term laterite. *Soil Sci. Soc. Amer. J.* **17**(2001): 102-108.

Reimer, T.O. 1986. Alumina-rich rocks from the Early Precambrian of the Kaapvaal Craton as indicators of paleosols and as products of other decompositional reactions. *Precambrian Research.* **32(2-3):** 155-179.

Rengasamy, P., Sarma, V.A.K., Murthy, R.S. and Murti, G.K. 1978. Mineralogy, genesis and classification of ferruginous soils of the eastern Mysore Plateau, India. *J. Soil Sci.* **29(3):** 431-445.

Retallack, G. 1984. Completeness of the rock and fossil record: some estimates using fossil soils. *Paleobiology*. **10(1):** 59-78.

Roy, A.B. 1988. Stratigraphic and tectonic framework of the Aravalli Mountain Range. *Mem. Geol. Soc. Ind.* **7:** 3-31.

Schellmann, W. 1986. A new definition of laterite. In *Lateritisation processes*, *Memoir of the Geological Survey of India, Vol.* **120:** 11-17.

Schmidt, P.W., Prasad, V. and Ramam, P.K. 1983. Magnetic ages of some Indian laterites. *Palaeogeography, Palaeoclimatology, Palaeoecology*. **44(3-4):** 185-202.

Singh, B. 1996. Why does halloysite roll? —A new model. *Clays and Clay Minerals*. **44(2):** 191-196.

Sinha-Roy, S., Mohanty, M., Malhotra, G., Sharma, V.P. and Joshi, D.W. 1993. Conglomerate horizons in south-central Rajasthan and their significance on Proterozoic stratigraphy and tectonics of the Aravalli and Delhi fold belts. *Journal of Geological Society of India (Online archive from Vol 1 to Vol 78)*. **41(4):** 331-350

Wilding, L.P. and Lin, H. 2006. Advancing the frontiers of soil science towards a geoscience. *Geoderma.* **131(3-4):** 257-274.

Wilson, M.J. 1987. X-ray powder diffraction methods. In (Wilson, M.J. Ed.), *A Handbook of Determinative Methods in Clay Mineralogy*, Chapman & Hall, New York, pp.26-98.

(Received: 20 November 2019; Accepted: 10 February 2020)

Clay Research, Vol. 38, No. 2, pp. 63-74 (2019)

Petrological Characterization of Residual Quartzites Associated With Kadavur Anorthosite Complex, Tamil Nadu, India

KUMAR R. S., ASAIMANI S. JUSTINE ANTONY K. *, RAJKUMAR P. AND ARAN CASTRO A. J.

Department of Earth Sciences, Annamalai University, Tamil Nadu, India

***Abstract**: Kadavur Anorthosite Complex (KAC) is composed of undeformed plutonic intrusive emplaced into a complex structural set up made up of quartzite. Many more studies have been carried out on the KAC as it is a typical massive anorthositic pluton with its associated rocks ranging from gabbroic to anorthositic rock with chilled marginal contact with the structural quartzites. It is a convoluted geological terrain to delineate its genesis and lithological categorization. In the field the quartzites occur as compositional banding with gneissic fabrics and at places it has witnessed the recrystalline granulose texture. Here in this study a detailed field and petrological correlation have been carried out to understand its characterization and comprehensive lithological grades. The detailed petrological studies indicate that the quartzite type rocks can be classified petrologically with four distinct variations of rocks of its kind. The constituent minerals in the quartzite such as sillimanite, ferruginous minerals and mica group of minerals i.e biotite and muscovite are the prime factors for the classifications of the said rock.*

Keywords: Classification of minerals; Kadavur Anorthosite Complex (KAC); mineral assemblage; petrography; quartzite.

The Kadavur Complex (KC) situated in one of the largest exposed Neoproterozoic granulite terrain has been a subject of well known research due to the exceptional geologic history. It occurs as a distinct structural feature in the Southern Granulitic Terrain (Asaiman *et al.,* 2020). This study focuses on the petrological characterisation of the quartzites and its type rocks occurring in the Kadavur area. The study area, Kadavur Complex, occurs as a distinct structural feature known as Kadavur Structural Complex (KSC) in the northern part of Madurai block of Southern Granulite Terrain (SGT). The Kadavur Structure Complex hosts the Kadavur Anorthosite Complex which is composed of anorthosite, anorthositic-gabbro, gabbroic anorthosite, quartzite and chilled margined gabbro. Quartzites are the major rock type occur as residual hills forming the structural complex and encircle the Kadavur basin around the anorthositic and gabbroic rock formations. Due to the exceptional structural setting of the area, it is known as Kadavur basin and structurally termed as Kadavur Structural Complex (KSC). Generalized petrological descriptions of Southern Granulite Terrain have been published in many works in which Kadavur Complex has been noticeably explained that mainly included the composition of rock types and its structural aspects. SGT is composed of multiple blocks divided by shear zones. Among them, Madurai block remains peculiar due to the distinct magmatic and metamorphic history. The Kadavur structural complex falls in the northern part of Madurai block. The block can further be divided into eastern and western block which is differentiated by north south trending thrust according to Kalian *et al.,* (1979). Northern block can also be differentiated from the southern block

***Corresponding Author's email:** justinekantony@gmail.com
DOI:10.5958/0974-4509.2019.00003.2

based on metamorphic grade, change in structural style and lithological variations which can also be observed. Many studies have been carried out to delineate the structural and petrological history of the KC, but adequate geological data that can be used to differentiate and understand the Complex is lacking and significance of which are not well understood as well. As the residual hills are mainly composed of quartzite, understanding the geological aspects and differentiating the quartzite type rocks using the petrological studies in the area are important which will help to know the mineral assemblages and textural characteristics of the quartzite and its type rocks.

GEOLOGICAL SETTING

Regional Geology

The Kadavur complex is situated in the Madurai Block (MB) that occupies the largest portion of the Southern Granulite Terrain (SGT) and represents a composite middle to lower crustal domain (Figure 1). Madurai block has a fundamental part in characterizing the Proterozoic

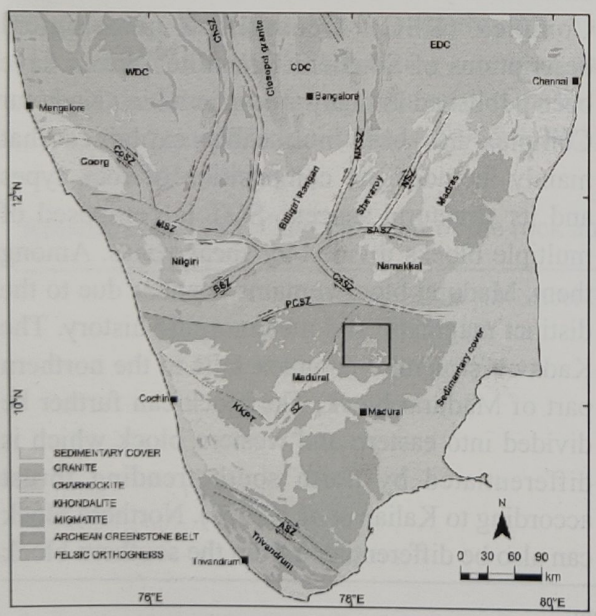

Fig. 1. *Location map of the study area modified after Ishwar-Kumar et al., (2013)*

geodynamic evolution of the SGT due to its distinct deformational activities and metamorphic processes occurred in the block which also gave rise to the formations and occurrence of Kadavur Complex. The block is also differentiated by many shear zones formed which acted a key role in the geological history of the terrain. The Kadavur complex has therefore showcased the characteristics of the Madurai block including multiple deformations and metamorphic activities.

Geology of Kadavur complex

The study area Kadavur is located in the north of Madurai block, at 10°35'03.67"N, 78°11'44.64"E in the state of Tamil Nadu, Southern part of India. It falls about 35 km south of the Palghat Cauvery Shear Zone (PCSZ). Kadavur is a taluk located in the Karur district of Tamil-Nadu state, India. Petrologically the Kadavur Complex is composed of anorthosite, anorthositic-gabbro and gabbroic anorthosite at the center or core of the basin and at the margin composed of chilled marginal gabbro and quartzite forms around them in the area (Subramaniam A.P. 1956, Amithabha Sarkar *et al.,* 1987) (Figure 2). The distinct occurrence of anorthositic rocks in the study area is a geologically an interesting feature which attracts many geologists in the world. Due to the contrasting structure of the Kadavur area formed by the anorthositic and gabbroic rocks encircled by the residual hills of quartzite and its associated rock, the area is termed as Kadavur Structural Complex (KAC) (Asaiman S *et al.,* 2020). And it measures approximately 22 km from eastern periphery to western end and 17 km northern to folded zone to south upto Ayyalur. Field observations made during the detailed field work carried out in the study area show that the rock exposures exhibit foliations, lineations and assemblages of essential minerals and selected samples were collected for detailed petrographical observations.

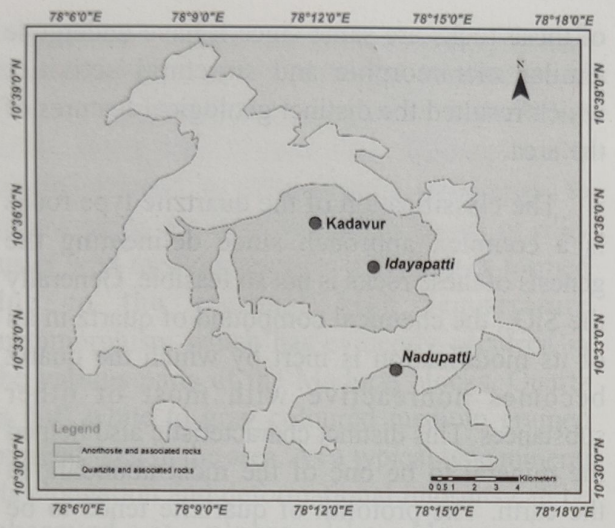

Fig. 2. *Geological map of the study area modified after Kumar R.S. (2000)*

Structural Framework

The study area retains complex structural history and hence it has undergone several phases of deformations during its formation. Kadavur structural complex is composed of well deformed rock which preserves structural characteristics even in the quartzite and other associated lithologies (Figure 3). Senthil Kumar R.(2000) stated that the quartzite occurs as distinct circular hill ridges and form the oldest rock type of the area, which is evidently observed in the field. Strong structural features like foliations, mineral lineations and types of folds are observed in the majority of the country gneissic rocks and quartzites in the the structural basin of the study area. As quartzite occurs at the peripheral part of the basin and due to the resistance towards weathering occurs as residual hills. These residual quartzites preserves complex deformation and structural characters, it has not exhibited the specific structural characters even though the rock possesses foliations. At some places the anorthosite suit of rocks also witnesses the latter deformational regime. These anorthosite is intrusive into the gneisses and contacts wherever exposed shows some degree of silicification marked by the appearance of quartz intrusion K-feldspar and formation of myrmekite (Arumugham M. *et al.,* 1998). The authors also suggested that the anorthosite around the Kadavur Complex is a diapiric intrusion which stated that the anorthosite is forced into the brittle overlying rocks of quartzite. Plavsa D *et al.,* (2015) has differentiated the quartzite of Kadavur complex as foliated strongly foliated quartzite. The study of regional scale has given classical evidence for a poly deformation history which include refolded folds and variable mineral lineations. The KSC has witnessed minimum of three generation of regional deformation resulting asymmetric fold and fabric suggesting the impact of dextral and sinistral impacts on the quartzites. Overprinting of structural deformations can be well noted in the quartzite complex.

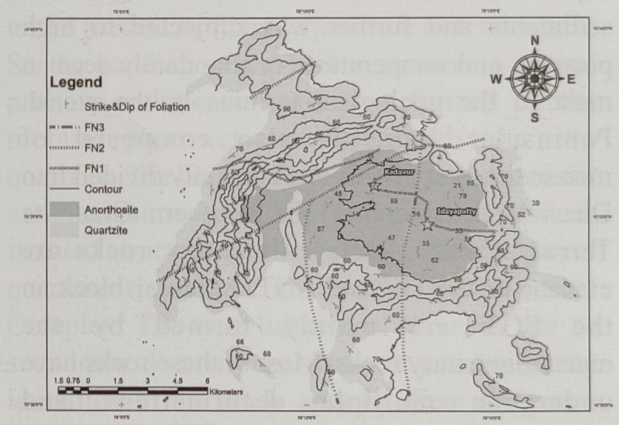

Fig. 3. *Structural map of the study area (Asaimani S. et al., 2020)*

Petrology and Mineralogy

Introduction

The Kadavur Structural Complex is predominantly composed of quartzite. It forms the part of the Proterozoic Madurai block of Southern Granulite Terrain in the peninsular India. The Madurai block is bounded by Palghat Cauvery Shear Zone in the north, Trivandrum block and Nagercoil block in the south part. The formation and geological history of the Madurai block remains peculiar to other terrains in the

peninsular India. It has undergone multiple types of deformations and metamorphism and has recorded extreme crustal metamorphism at ultrahigh temperature conditions. Due to the typical formations, Madurai block is characterized by the presence of metasedimentary rocks and charnockites (Santhosh *et al.,* 1992; Bartlett *et al.,*1995; Jayananda *et al.,* 1995a). As Kadavur Complex is mainly composed of metasedimentary rocks of quartzite, a detailed study of quartzite has to be carried out. To attain this, understanding the metasedimentary rocks in Madurai block is necessary for the study.

Metasedimentary rocks of Madurai block

Metasedimentary rock, formed due to the depositional and solidification processes of the sediments and further was subjected to high pressure and temperature, is abundantly seen in most of the geological terrains in the world. Peninsular India is also composed of metasedimentary rocks and is mainly divided into Dharwar Craton (DC) and Southern Granulite Terrain (SGT). Metasedimentary rocks are evident in the DC and SGT. Madurai block in the SGT are mainly formed by the metasedimentary rocks. Most of these rocks have undergone multiple deformations and metamorphic activities at different stages.

Metasediments that host and form the structure of Kadavur is composed of quartzite which occurs as residual hill where the other country rocks like hornblend-biotite gneiss are found in the ground level of contour.

Classification of quartzite complex

Quartzite is a major rock type in Kadavur and seen at peripheral part of the area composed of residual hills. The Kadavur quartzites are found as compositional banding rocks. It is exposed mainly in the hill parts of Kadavur Complex. Depending on the petrological features the quartzite can be broadly classified. The protolith of these rocks are same since it have undergone similar metamorphic and structural activities which resulted the distinct geological features of the area.

The classification of the quartzite type rocks is a complex approach since delineating the genesis of these rocks is not so feasible. Generally the SiO_2, the chemical compound of quartz in all of its modification is inert by which the quartz becomes nonreactive with most of other substances. This distinct characteristic also helped the mineral to be one of the most abundant in the earth. The protolith of quartzite tends to be same due to the geological processes. Most quartzites form during the orogeny mainly occurred at convergent plate boundaries. In the light of the mountain-building processes, the sandstone which is mostly composed of quartz is metamorphosed into quartzite when it undergoes deep burial during the process. Since these processes occur at the plate boundaries, the newly formed rocks experience folding and faulting due to the compressional forces and it results in thickening the crust into the mountain ranges. Hence, this is main reason for the occurrence of quartzite in the residual hill seen as distinct relief around the Kadavur Structural Complex.

So these quartzites formed by the former processes tend to exhibit the discrete characteristic features. It is mainly based on the compositional differentiations by which the quartzites possess different mineral as an essential or dominant component. Due to the presence of quartz as essential minerals in the quartzite, the classification of quartzite was attempted based on the occurrence of other accessory minerals present considerably from the type locations.

Sillimanite-quartzite

It is a medium to coarse-grained buff coloured rock which is mainly composed of quartzite and sillimanite minerals. In the field the sillimanite quartzite exhibits well defined foliation. It also

exhibits well aligned mineral lineation. Though the sillimanite cannot be identified with the naked eye they are found to be aligned with the foliar fabric of the rock (Figure 4A). Sillimanite, the silicate mineral is often seen as colourless to yellow-green colour. It appears as greasy or silky luster with medium specific gravity. It is formed due to the regional high temperature metamorphism which has evidently occurred in the various parts of the Madurai blocks. Quartz is buff white to gray coloured medium grained mineral seen in the area. As a typical type mineral its elongation and deformational imprints can be observed at places like Mamanniyur, Mamanathupatti and Valayapatti villages (Sentil Kumar R. 2000).

Muscovite-quartzite

It is fine to medium grained rock and mainly composed of quartz and muscovite minerals. It is massive in nature in which muscovite minerals are seen colourless and yellow-brown coloured. Excellent cleavage in one direction is the distinguishing feature of the muscovite in hand specimen as well as in the field. It shows white streak and non-metallic luster. It can be easily identified by splitting the mineral into thin flexible transparent sheets. The rock is also termed as fucsite quartzite due to the presence of chromium rich variety of the mineral in the muscovite group (Figure 4B). It is light to grey to pale greenish coloured rock with alternating bands of quartz and muscovite minerals. Among the minerals present in the rock, the muscovite minerals sometimes define the orientation and foliation direction of the rock which occasionally shows gneissic texture.

Biotite-quartzite

It is medium to coarse grained rock mainly composed of quartz and biotite mineral (Figure 4C). Boitite may also be seen as tabular texture in the rock. It is seen as black to green and brown-black coloured with the excellent cleavage as the distinguishing properties. It also possesses low hardness and specific gravity. The linear arrangement of the biotite minerals exhibited in the rock characterizes the foliation of the rock and occasionally indicate that the rocks show gneissose texture. It can also be termed as banded biotite quartzite since the boitite is seen as banded structure in the rock. A minimal amount of garnet as well as muscovite can also be observed in the rock.

Banded ferruginous quartzite

The quartzite of the type is common in the study area. It is fine to medium grained reddish brown coloured rock exhibiting the banded structure (Figure 4D). The distinct appearance of banding and colour occuring in the rock is due to the presence of quartz and iron rich minerals.. So the banding of the rock represents a typical primary sedimentary structure formed by the metamorphic activities of sandstone into quartzite. The banded ferruginous quartzite occur as continuous layer of formation or seen as isolated structures all along the circular ridges of quartzite type rocks in the Kadavur Structural Complex. The type location of the rock can be seen near Ponnaiyaru dam. It can be easily identified in the study area by their distinctive appearance of alternative banding with brownish colour and characteristics of weathering. The contrasting colour of the rock is due to the presence of iron rich minerals and specific mineral identification of the iron oxide minerals can be done by the petrographical studies.

In general, quartzites are metamorphic rocks in which quartz is the essential mineral (Figure 4E). Quartzites are the metasedimentary formation of the region that may be derived from siliceous sediments. Hence quartzite occurs as patches with high relief as they are resistant to the weathering. As the quartzite have undergone multiple processes of geological activities both in metamorphic and structural aspects, the rock have resulted structural and textural

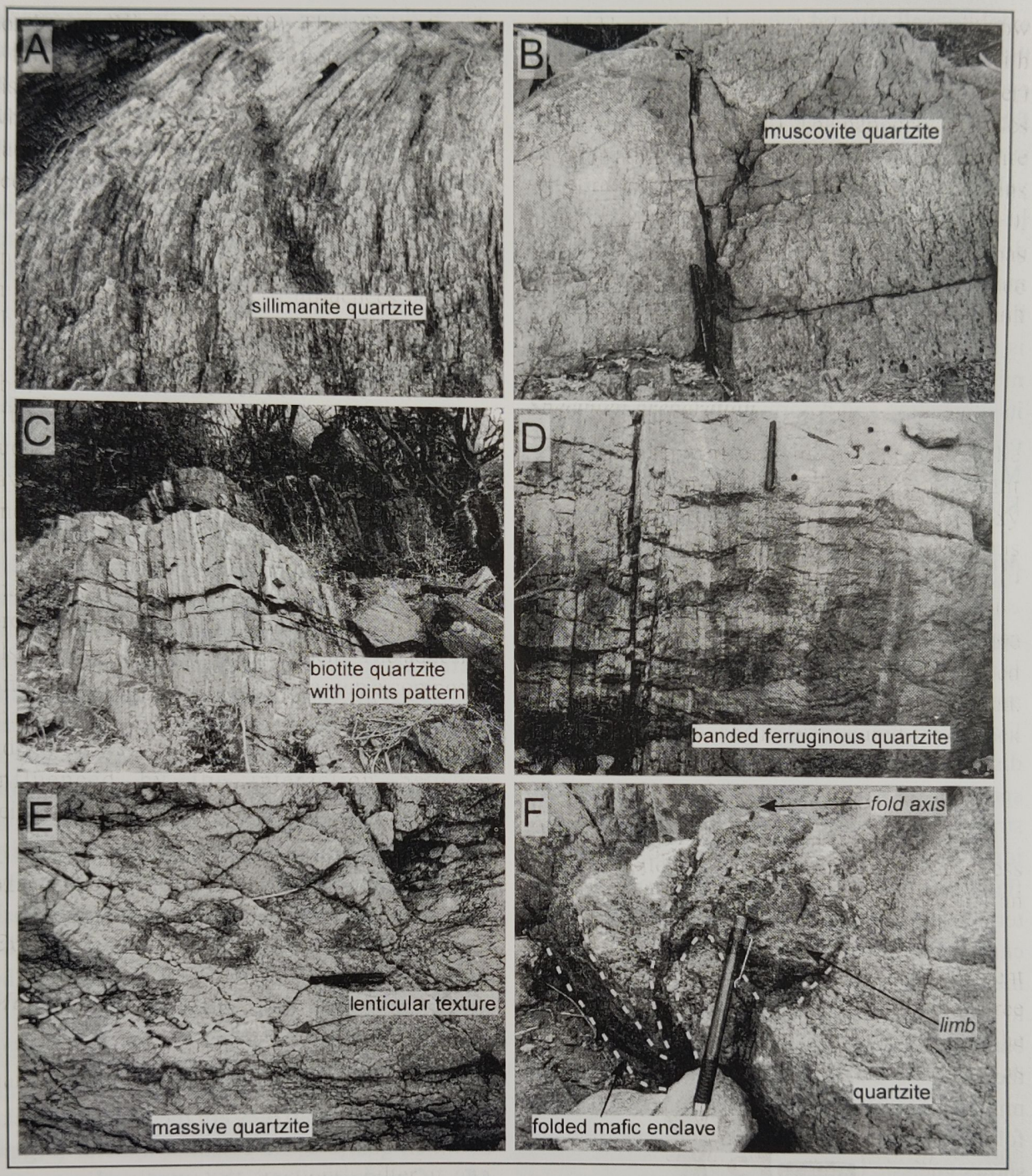

Fig. 4. *Field occurrence and rock type photographs of representative samples. A) Foliated Sillimanite quartzite. B) Muscovite quartzite. C) Biotite quartzite with joints pattern. D) Banded ferruginous quartzite .E) Quartzite showing lenticular texture .F) Quartzite with folded mafic enclave*

characteristics. They have been deformed as folded, faulted and even shearing in the area (Figure 4 E & F). Weathering is a common noticeable process exhibited in the study area that the rock shows the typical two sets of joints pattern causing the rise of rate of weathering.

Result and Discussion

Petrography of rocks

Petrography enables the optical consideration of quartzite and its type of rocks exposed in Kadavur Complex which helps to attain the information about the mineral assemblages and textural characteristics of the rock. It even delineates the evolution of the rock and the stages of its formation. In the light of the petrological studies, classification of quartzite based on the different textures and accessory minerals present in the rock has been attempted. Many classical work have been carried out describing the generalized description of Southern Granulite Terrain and further Madurai block (Rama Rao, 1945; Pichamuthu, 1979; Howie, 1955; Subramanian, 1967). And more detailed petrography and its subsequent mineral chemistry have also published in recent works (Raith *et al.,*1983; Chacko *et al*., 1987; Brown *et al*., 1992; Ravindrakumar and Chack., 1994; Srikandappa., 1993, 1996; Santhosh, 1996; Mohan, 1996; Satish Kumar, 2000; Ravindra Kumar 2005). But very less studies have been carried out concentrating on the north eastern part of Madurai block especially quartzites of Kadavur complex. And none of the given works helps to attain the complete information due to the complexity of the study area Kadavur in structural and petrological aspects as well. So the present study aims to emphasize the important petrographic features of the quartzite and its type rocks in the study area.

Microscopic observations were made and photomicrographs were prepared using Olympus BX53 petrological microscope attached with a camera. It is equipped with double illuminators for viewing the thin sections under both refractive and reflective mode. An imaging software Cellsens was used along with this for snapping quality images of the sample sections. Detailed petrographic analysis of major rock types were carried out. Number of thin sections covering quartzites, its type of rocks and other adjacent rock types were prepared by conventional methods. The petrography of each thin section was studied under the petrological microscope.

Sillimanite-quartzite

The medium to fine grained massive rock with quartz and sillimanite are seen as essential minerals. Microscopic study indicates that the rock exhibits granulose texture in which sillimanite is observed as it is entrapped between the grains of quartz which shows equi-granularity (Figure 5 A & B). Sillimanite is seen as needle and tabular shaped which also exhibits as inclusions and along the quartz grains such that the distinct appearance of the mineral helps to identify easily in the quartz matrix.

Sillimanite is found to occur nucleated around the quartz grain boundaries. In some of the sections the sillimanite occurs inside the quartz grain as well. It can be identified by pleochroic to non-pleochroic character of sillimanite and quartz respectively.

Mineral assemblages of the rock are

Qtz+ Sill+Mag+Zrn

The rock is composed essentially of quartz and sillimanite with minor amount of magnetite, ilmenite and zircon. The quartz is non-pleochroic and cleavage absent mineral showing wavy extinction in cross nicol. Zircon grains are present in very minimal amount which is also seen as elongated resemblance to the sillimanite mineral. Opaque mineral observed in the thin section of the rock is magnetite and ilmenite showing isotropic characters. Considering these characteristic features of the rock including the mineral assemblage and specific textures, the rock was classified as sillimanite quartzite.

Muscovite quartzite

The rock exhibits medium to fine grained euhedral to subhedral texture. It shows distinct

appearance of the minerals that quartz is seen as essential mineral and muscovite shows well formed crystals and pale green colour. The arrangement of muscovite minerals are seen as flakes. So the rock possesses granulose texture which has equi-granularity (Figure 5 C&D).

The mineral assemblages of the rock are

Qtz+Ms+Mag+Zrn

The granulose texture of the rock is defined by the presence of the essential mineral quartzite which is a non-pleochroic cleavage absent mineral. The muscovite shows perfect cleavage and parallel extinction. Magnetite and ilmenite rarely seen are the opaque minerals in the thin section. High relief, strong interference colour and elongated to rounded shape help to identify zircon easily which is a very common accessory mineral in a vast type of rocks. The rock is so termed as muscovite quartzite due to the presence of muscovite mineral preferably higher amount.

Biotite quartzite

The microphotographs of the thin section shows it is granulose texture formed due to the composition of equidimentional minerals. It shows moderately to strong deformed and non-foliated appearance. Biotite sometimes shows linear arrangement in the matrix. The mineral assemblages of the rock are:

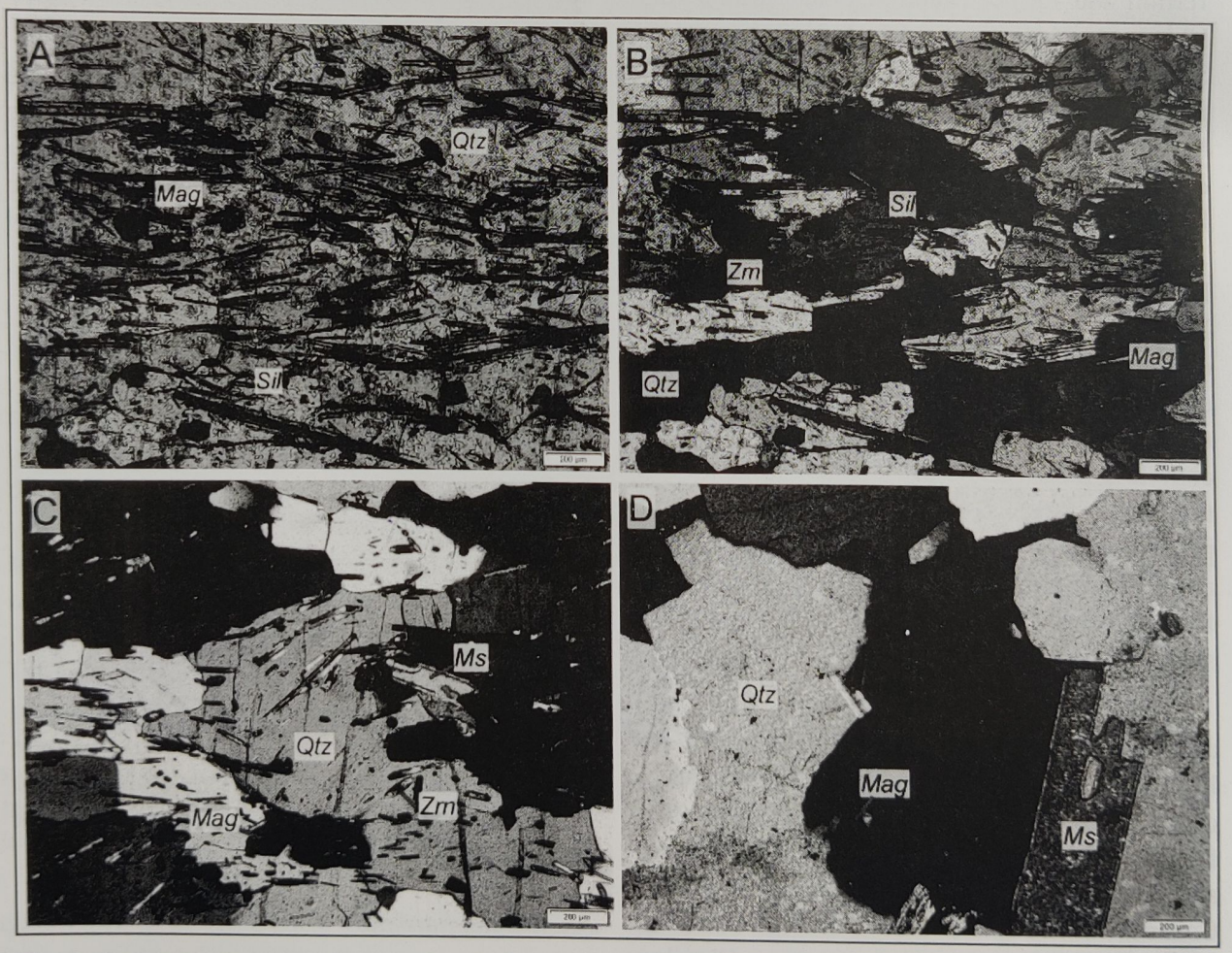

Fig. 5. *Representative microphotographs of mineral assemblages and textures of the samples. A & B) Sillimanite quartzite exhibiting minerals present and metamorphic textures in open and cross nicol respectively. C & D) Muscovite quartzite with muscovite mineral embedded in quartz as matrix, seen in open and cross nicol.*

Qtz+Bt+Ms+Op+Zrn

The rock is essentially composed of quartz. Biotite is also observed as flakes formed as essential mineral. Quartz is colourless, cleavage-absent, non pleochroic, low relief and refractive index is 1.55, Anisotropic, wavy extinction, low interference colour. Biotite is brown to black coloured mineral with perfect cleavage seen as micaceous cleavage (Figure 6 A&B). Opaque mineral seen in the thin section is magnetite and zircon is observed due to the high relief and elongated shape. Since biotite is seen as considerable amount in the thin section of the rock, it is termed as biotite quartzite.

Banded ferruginous quartzite

It is a common rock type seen in the study area. The thin section of the rock shows the minerals are arranged in a linear form from coarse to fine grained minerals. The rock exhibits granulose texture. The grained texture results phaneritic texture in the rock. The grains are subhedral that partial formation of crystal faces are seen (Figure 6 C&D).

The mineral assemblages of the rock are,

Qtz+Rt+Zrn+Op

Quartz is the essential mineral in the rock. It is an anisotropic mineral with non-pleochroic and

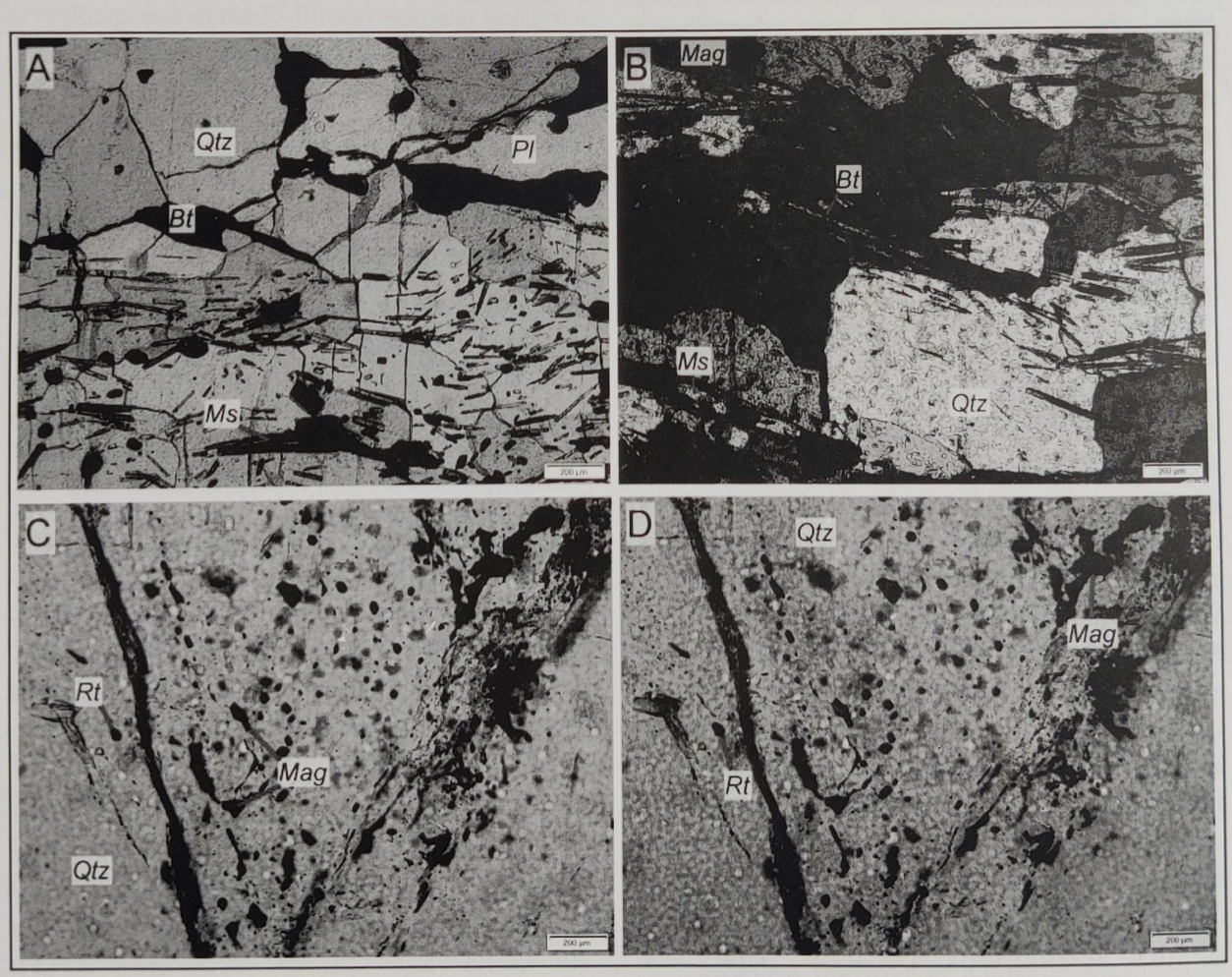

Fig. 6. *Representative microphotographs of mineral assemblages and textures of the samples. A & B) Biotite quartzite exhibiting the minerals present with the texture in open and cross nicol respectively. C & D) Banded Ferruginous Quartzite with quartzite as matrix mineral and magnetite as ferruginous mineral seen in open and cross nicol system respectively.*

colourless mineral. The accessory minerals included in the rock are opaques which are magnetite seen as small inclusions within the quartz grain. Rutile seen as deep red to brown coloured with high relief is also observed as small grains appeared as inclusions within the quartz grain. The arrangement of the minerals seen in the thin section of the rock supported to be termed and named as banded quartzite.

Conclusions

Extensive petrographical studies of quartzites and its types in the Kadavur Structural Complex in the northern part of Madurai block of SGT have been attempted for identifying their mineral assemblages and textural characteristics for further characterization of those residual rocks. The quartzite which occurs as residual hills are complex in its composition and characterization thus making it difficult to classify. They generally occur at the places as compositional banding of rocks. These compositional bands vary from place to place in the study area. At places two of these types of classified units are found together where some of the classified unit dominate at certain localities. Based on the detailed petrographical studies the contrasting four broad units of quartzite rocks have been identified. The quartzite which is composed of sillimanite other than quartzite in the rock is classified as Sillimanite-quartzite. Muscovite minerals are seen along with quartz and the rock is termed as Muscovite-quartzite. A type of quartzite possesses biotite in a considerable amount which is classified as Biotite-quartzite. And presence of ferruginous minerals is observed as arranged in the linear form along with the typical composition of quartzite. This type of quartzite is classified as Banded ferruginous quartzite. Therefore petrographical studies of the different types of residual quartzite in the study area are important to establish the textural characteristic properties and their mineral assemblages of various types of its kind.

Acknowledment

The Author would like to thank the unknown reviewers for their careful and critical review and their valuable suggestions as the manuscript. This research work was supported by UGC- MRP Project (MAJORGEOL;2013-19006), Utilization of the lab facilities for this work was supported by DST-SERB Project SERB (Letter No.SB/ EMEQ-489/2014). ISS Sevapur is thanked for providing boarding and lodging during the stay in the field

References

Arumugam, M. and Senthilkumar, R. 1998. Is anorthosite around Kadavur (Karur district, Tamil Nadu)—A diapiric intrusion? *Indian Mineralogist.* **32:** 35.

Asaimani, S., Kumar, R.S., Aran Castro, A.J. and Justine Antony, K. 2020. Preliminary characterization of Multi-deformed Kadavur Structural Complex, Tamil Nadu. *Infokara Research.* **9** (3) : 866–875. DOI:16.10089. IR.2020.V9I3.285311.3578

Bartlett, J.M., Harris, N.B.W. Hawkesworth, C.J. and Santosh, M. 1995. New isotopic constraints on the crustal evolution of South India andPan-African granulite metamorphism. In: M. Yoshida and M.Santosh (eds). India and Antarctica during the Precambrian. Geological Society. India, **34** : 391-397.

Ghosh, J.G., de Wit, M.J. and Zartman, R.E. 2004. Age and tectonic evolution of Neoproterozoic ductile shear zones in the Southern Granulite Terrain of India, with implications for Gondwana studies. *Tectonics.* **23(3)**: TC3006. https://doi.org/10.1029/ 2002TC001444.

Hussain, S.M., Narayana, B.L. and Naqvi, S.M.

1996. Geochemistry anorthosites from Kadavur, Tamil Nadu. *In* N. G. K. Murty,and V. Ram Mohan (Eds)., Charnockites and granulite facies rocks, Geologists Association of Tamil Nadu (pp. 339–349).

Jayananda, M., Martin, H., Peucat, J-J and Mahabaleswar, B. 1995b. The late Archaean crust mantle interactions: Geochemistry of LREE enriched mantle derived magmas. The Closepet batholith of southern India. *Contributions to Mineralogy and Petrology,* **Vol. 119**, pp. 314-329.

Kooijman, E., Upadhyay, D., Mezger, K., Raith, M.M., Berndt, J. and Srikantappa, C. 2011. Response of the U-Pb chronometer and trace elements in zirconto ultrahigh-temperature metamorphism: the Kadavur Anorthosite Complex,southern India. *Chemical Geology* **290:** 177–188.

Maheswaran, S.U., Anbazhagan, S., Tamilarasan K., Kasilingam, C. and Chinnamuthu, M. 2019. Lithology and Structural Mapping of Kadavur Basin, Tamil Nadu, India,Using IRS P6 LISS III Satellite Data _ Indian Society of Remote Sensing 2019

Naik, H. and Mukherjee, A. 2014. Specialised Thematic Mapping in Parts of Kadavur Structural Basin, Dindigul, Karur and Tiruchirapalli Districts, Tamil Nadu, Unpublished GSI Report.

Plavsa, D., Collins, A. S., Foden, J. D. and Clark, C. 2015. The evolution of a Gondwanan collisional orogen: A structural and geochronological appraisal from the Southern Granulite Terrane, South India. *Tectonics* **34:** 820–857 [doi:10.1002/2014TC003706].

Santosh, M., Kagami, H., Yoshida, M. and Nanda-Kumar, V. 1992. Pan-African charnockite f ormation in East Gondwana; geochronologic Sm-Nd and Rb-Sr petrogenetic constraints. *Bull. Indian Geological Association.* **25 :** 1-10.

Sarkar, A. and Bose, M. K. 1987. Geology of Kadavur complex, Tamil Nadu, *Recent Researches in Geology*. **13**: 97-107.

Senthilkumar, R. 1999. Geological-setting, petrology, mineralogy and geochemistry of anorthosite and related rocks in and around Mammaniyur, adjoing Kadavur, Dindigual-Karur districts, Tamil Nadu, South India. Ph.D thesis Annamali University.

Subramaniam, A. P. 1956. Petrology of the anorthosite–gabbro mass at Kadavur, Madras, India. *Geological Magazine/* **93(04):** 287–300.

Teale W. 2010. Structure, geochology and geochemistry of Kadavur dome, Southern India. University of Adelaide, Ph.D thesis (unpublished) p 125.

Teale, W., Collins, A.S., Foden, J., Payne, J.L., Plavsa, D., Chetty, T.R.K., Santosh, M. and Fanning, M. 2011. Cryogenian (~830 Ma) mafic magmatism and meta-morphism in the northern Madurai Block, southern India: a magmatic link between Sri Lanka and Madagascar? *J. Asian Earth Sciences* **42:** 223–233.

Uma-Maheswaran, S., Arivazhagan, S. and Sisodia, M. S. 2011. Remote sensing study of Kadavur structure—A possible analog site for lunar highland region-preliminary approach. In Conference on planetary sciences and exploration, 12–14 December 2011, PRL, Ahmedabad, India. Abstract. p. 22.

Vinodkumar, M., Kumar, R.S., Rajaprian, K., Singh, K. 2013. Petrography and major geochemical studies of Anorthosite, Kadavur and adjoining area, Tamil Nadu, India, *Intern. Res. J. Earth Science* **1(5)** : 15-22.

Vinodkumar, M., Kumar, R. S., Rajaprian, K. and Singh, K. 2014. Mineralogical studies of plagioclase feldspar in Kadavur Anorthosite Complex, Tamil Nadu. *Intern. J. Adv. Geosciences* **2:** 31-37.

Vinodkumar, M., Kumar, R. S., Rajaprian, K. and Singh, K. 2013. Geological and petrological studies of pegmatites rocks of in and around Kadavur, Karur district, Tamil Nadu, 2, 182-191.

Windley, B.F. and Selvan, T.A. 1975. Anorthosites and associated rocks of Tamil Nadu, Southern India. *J. Geological Soc. India* **16:** 209–215.

(Received: 19 April 2020; Accepted: 14 June 2020)

Clay Research, Vol. 38, No. 2, pp. 75-82 (2019)

Thermochemical Conversion of non-Food Feedstock of Moringa *oleifera* Seed Bio-Oil to the Biodiesel and its Blends with n- Butanol-diesel and Utilization of Glycerol Obtained as By-product

HARISH CHANDRA JOSHI [1,*], JITENDRA SINGH [2], AND AISHWARYA AGGARWAL [2]

[1] *Department of Chemistry, Graphic Era (Deemed to be) University, Dehradun, Uttarakhand, India*
[2] *Department of Chemistry, Uttaranchal University, Dehradun, Uttarakhand, India*

Abstract *- The Present work aims to produce of biodiesel from Moringa oleifera by Thermochemical conversion (TCC) and purification, utilization of glycerol. 30% (w/w) bio oil and high yield of biodiesel was achieved by the TCC process. The execution of biodiesel was expanded by the mixes with butanol-diesel (Biodiesel+Butanol+Disesl) in various extents. The obtained biodiesel and its blends were characterised by ASTM. Crude glycerols were obtained as a by-product from the methyl ester of Moringa oleifera seeds.* H_3PO_4, H_2SO_4, *HCl and* HNO_3 *were used for the purification of crude glycerol. Purified glycerol was characterised by the density, alkalinity, ash content, Moisture content, FT-IR etc. study confirmed the purification and formation of glycerol.*

Keywords: Bio oil; Biodiesel; Biofuel; *Moringa olifera*; Thermochemical Process.

Biodiesel is highly biodegradable, renewable fuel than the fossil fuel, can be used directly in diesel engine without any engine modification (Dwivedi and Sharma 2016). Biodiesel is a mixture of monoalkylated esters of the long chain fatty acids, which can be produced by different feedstocks such as vegetable oils, animal oils, edible or non-edible seeds with acid, base, enzymatic or heterogeneous transesterification process with methanol (Jon, 2005; Knothe, 2005; Joshi and Negi, 2017). Biodiesel can be used unadulterated (Foglia, Jones & Phillips 2005; Hu *et al.,* 2004) or blended with petro diesel, butanol or alcohols lead to reduces the emission characteristics and increases the engine performance without any engine detoriation (Qi *et al.,* 2009; Aydin and Ilkilic, 2010; Kumar *et al.,* 2018). The arrangement of biodiesel and cost is straightforwardly reliant on the level of oil substance of the feedstock (Bozbas, 2008; Joshi and Kumar, 2016).

Thermochemical conversion (TCC) is a process in which biomass is converted in hot compressed water to a liquid crude bio oil (Yunuskhan *et al.,* 2014). Literature reported that the thermochemical (TCC) or hydrothermal liquefaction (HTL) technique is the most effectively for the production of biodiesel from algae (Demirbas, 2011). Thermochemical or liquefaction extracts the more bio oil from the high lipid-content biomass.

Crude glycerol is obtained as a principle by-product from biodiesel, which is approximately 10% wt of vegetable oil (Dasari *et al.,* 2005). Glycerol was produced amid the transesterification after that detachment procedure in which the base layer of the unrefined glycerol, that contains water, salt, seed hues and also with the traces of triglycerides (Hajek and Skopal, 2010). Glycerine, or glycerol, finds several applications in the manufacturing of surfactants, solvents, polymers, medicines, cosmetics foods and industrial

***Corresponding Author Email :** joshiharish86@gmail.com
DOI:10.5958/0974-4509.2019.00004.4

purposes (Hajek and Skopal 2010; Tan, Aziz and Aroua 2013; Pagliaro 2013). The *Moringaceae* is a solitary sort group of oilseed trees with 14 known species of these, *Moringa oleifera*, which runs in range from 5 to 10 m, is the most broadly known and used (Sousa *et al.,* 2014; Sengupta and Gupta, 1970). The *Moringa oleifera* are most accessible in northwest India, Malaysia, Bangladesh, Africa, South America and Arabia, and so on (Morton, 1991). The *M. oleifera* contain 70% of fatty acids (Du *et al.,* 2013).

Materials and Methods

Material

Seeds of *M. oleifera* were collected from the local areas of Uttar Pradesh, India. The Chemicals were of an analytical reagent grade, that is, n-hexane, methanol (99.5%), butyric acid, Nitric acid, Sulfuric acid, hydrochloric acid, ethanol (99.5%), potassium hydroxide (85%), Wij Solution, purchased from Sigma Aldrich.

Thermochemical Conversion (TCC), Transesterification, fatty acid profile

In thermochemical conversion (TCC) the *M.oleifera* seeds were dried and crushed into fine grined powder. The fine grined powder (2.5g), desired amount of deionised water and Na_2CO_3(2 wt. %), were placed in stainless steel reactor. The reactor was kept in muffle furnace with temperature range 250 ^{0}C- 350 ^{0}C, pressure 5-10 Mpa andtime 30-60 minutes in the absences of oxygen (Wanga *et al.,* 2013; Ataban *et al.,* 2013). After this reactor was opened and pour the content in beaker and add n-hexane for the recovery of all product fractions. Filter it and reject the solid biochar (residue). The liquid bio oil was placed in rotatory evaporator at 40 ^{0}C for 2 hrs for the removal of n hexane.

A three neck round bottom flask were used as a reaction reactor for the transesterification process. The aggregate extricated bio oil were transesterified into FAMEs by potassium methoxide in the presence of CaO catalyst (activated) for 2.5 hrs (Kafuku *et al.,* 2010). Stored the methyl ester at -8 to -10 °C for the prevented the humiliation Fatty acid methyl esters (FAMEs) were analysed using GC-MS (Bale *et al.,* 2015).

The characterization of biodiesel and its blends like iodine value, saponification value, specific gravity, acid value, diesel index, FFA, high heating value, long chain saturation factor, specific gravity (40 °C), Corrosion etc obtained from *M.oleifera* seed oil were determined according to ASTM D-6571 specifications. Flash points were determined by Pensky-Martens closed cup apparatus. Cetane Number (CN), degree of unsaturation (DU), Oxygen stability (OS), Long Chain Saturation Factor (LCHF), Cold filter plugging property (CFPP), high heating value (HHV) affects the biodiesel quality and can be calculated by the empirical formulas (Kafuku *et al.,* 2010; Bale *et al.,* 2015; Agarwal and Rajamanoharan, 2009; Sanchez and Encinar, 2015)

Blend Preparation

This study focused on making blends of *M. oleifera* biodiesel in different proportions ratios to enhance the execution of fuel for the decrease of unsafe emissions. The proportions of blending is denoted as *M. oleifera* methyl ester 2% + n butanol 5% + diesel 93% (M2% + B5% + D93%), *M. oleifera* 5% + n butanol 10% + diesel 85% (M5% + B10% + D85%), *M. oleifera* 20% + n butanol 20% + diesel 60% (M20% + B20% + D60%), *M. oleifera* 50% + n butanol 45% + diesel 5% (M50%+B45%+D5%) (Khan *et al.,* 2016; Arora *et al.,* 2016; Kumar *et al.,* 2018). Blends were prepared using a hot plate with magnetic stirrer at room temperature for five minutes.

Separation, Purification and Characterization of Glycerol

The obtained by product of glycerol was melted at 45 ^{o}C- 55 ^{o}C. Acidified the crude

glycerol with H_3PO_4 (0.1N), HNO_3 (0.1N), HCl (0.1N) and H_2SO_4 (0.1N) until pH level reached 3-4. Three layers were obtained. Separated the middle layer of glycerol and neutralize with KOH (1N) (Nanda *et al.,* 2014; Priya and Brijesh, 2016). Neutralize glycerol was further treated by solvent extraction process followed by the addition of 0.2g charcoal.

Analysis of glycerol

The crude and purified glycerol were analysed by the density (at room temperature), pH (1 g sample in 50 mL of deionized water), Alkalinity, Soap content (Ishak and Ramlil, 2015; Ardi and Aroura, 2015; Pal and Chaurasia, 2016), Ash Content, UV-Visible spectrophotometer (λ 500 nm), FT-IR and GC-MS.

Results and Discussion

Physico-chemical analysis of Fatty acid biodiesel and its blends

The bio oil yield of 30wt % was achieved by the thermochemical conversion (TCC). The presence of GC-MS study of FAMEs exhibit that the presence of unsaturated fatty acids (poly) were the prime section of fatty acids obtained C22:2, C22:3 along with C13:1, C16:1 and C16:0 (Table 1).

The following results were obtained from physico-chemical study of the test methyl ester of *M.oleifera* (Table 2) as per the specification of Standard ASTM D6751.On the investigation of methyl ester, density and specific gravity of *M.oleifera* based biodiesel meet with the specification. Cloud, Pour point and flash point is ideal for the fuel conditions. Kinematic viscosity (KV) is quite high and shows the low oxidation stability, affect the engine performance and low load carrying potential (Franscisco *et al.,* 2010; Ramos *et al.,* 2009; Islam *et al.,* 2013). Iodine Value appraises the level of unsaturation showing polymerization of glycerides leads to the cold start property and complete combustion. Cold flow plugging properties (CFPP) are used to analyse performance of biodiesel at low temperature, once fuel cease to flow, CFPP is reached and engine will not be work (Hoekman, 2009). Above experimental data shows that the CFPP is -16 ^{0}C and oxygen stability is 6.8h specified the approximately good quality bio-based fuel. Moisture content is quite high and affects the calorific value and also the performance of engine. Corrosion test is negative for fuel. The calculated value of CN, DU, HHV, AV, SV give the information of biodiesel for the fluidity, fuel performance and ignition quality.

The characterization of blended biodiesel with n-butanol and diesel fuel were analysed

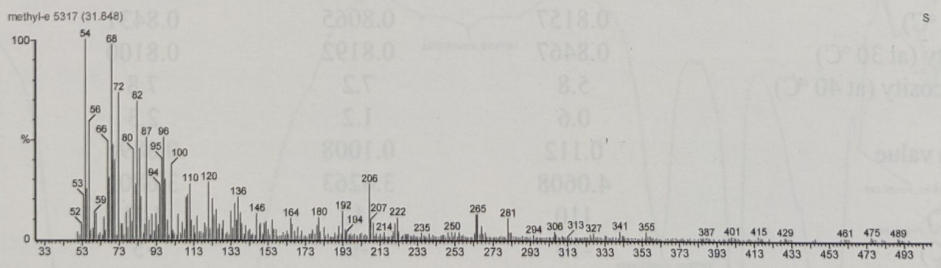

Fig. 1. *GC-MS analysis of Methyl Ester*

Table 1. *Fatty acid composition of M. oleifera seed oil*

Solvent	Fatty acid Composition (wt %)		
	PUFA	MUFA	SFA
Chloroform: Methanol (2:1)	68	30	20

(Table 3) and observed that the performance of M2+B5+D93 among all the fuel compositions. M2+B5+D93 is highly oxidation stability, minimise the gum forming, resistance to corrosion, easily fluidity and floats on water. The percentage composition of M2+B5+D93 is used

Table 2. *Physico-chemical Properties of the methyl ester*

Properties	Biodiesel	ASTM D 6751
Oil content (w %)	30	-
Density (at 30° C)	0.8745	0.875- 0.90
Free Fatty acids	4.024	0.020
Specific gravity (at 30° C)	0.87830	0.88
Kinematic viscosity (at 40° C)	29.29	1.9-6.0
Acid number	5	<0.8
Saponification value	0.112	0.80 (max)
Iodine value	9.8982	—
Flash point (°C)	110	100-170 °C
Cloud point (°C)	0°C	-15 to 16
Pour point (°C)	-9 °C	-3 to 12
Aniline Point (°F)	59	-
API Gravity	29.6066	-
Diesel Index	17.467	40
Ash Content	13	0.20
Moisture Content (%)	40	0.05
Copper Strip Corrosion	1	3 (max)
Sulfated ash (wt. %, max.)	0.001	0.020
Degree of Unsaturation (%)	47	-
Cetane Number (CN)	48	47 (Min)
Long Chain Saturation Factor (LCSF)	0.0	-
High Heating Value (HHV)	49.27	-
Cold Filter plugging Property (CFPP)	-16	-
Oxygen Stability (h)	6.8	3 (max)

Table 3. *Physico-chemical Properties of the Percentage of Blended Biodiesel with Butanol and Diesel*

Properties	M2+B5+D93	M5+B10+D85	M20+B20+D60	M50+B45+D5
Density (at 30 °C)	0.8157	0.8065	0.8431	0.8529
Specific gravity (at 30 °C)	0.8467	0.8192	0.8100	0.8212
Kinematic viscosity (at 40 °C)	5.8	7.2	7.8	8.9
Acid number	0.6	1.2	2.3	2.8
Saponification value	0.112	0.1008	0.0896	0.00899
Iodine value	4.0608	3.4263	3.6801	4.1442
Flash point (°C)	110	112	143	146
Cloud point (°C)	-10	-9	-5	-8
Pour point (°C)	-15	-14	-10	-10
Aniline Point (°F)	60.8	64.4	68.2	70
API Gravity	35.61	41.23	43.19	44.12
Diesel Index	21.650	26.552	29.455	29.55
Moisture Content (%)	2.3	2.5	3.1	1.6
Ash Content	0.01	0.01	3	2
Corrosion	1	1	3	3
Sulfated ash (wt. %, max.)	0.01	0.01	0.12	0.18

as a replacement to conventional diesel fuel among all the fuel compositions i.e. M5+B10+D85, M20+B20+D60, M50+B45+D5.

Characterization of Glycerol

Thompson and He (2012) reported that the crude glycerol contains 30% glycerol, 50% methanol, 13% soap, 2% moisture and 2-3 % other impurities. The obtained crude glycerol was found to be approximately 36% with low organic matter H" 50% and low ash content but high moisture contained (Table 4).

Table 4. Characterisation of Glycerol

Properties	Crude Glycerol	Purified Glycerol
Organic Matter (wt%)	50	1.11±0.02
pH	15	4
Color	Yellow-Brown	Colourless
Odour	Odourless	Odourless
Density (at 30 °C, g/mL)	0.9632	0.9632
Pour Point	11°C	-10°C
Alkalinity	10	0.5
Flash point	60°C	91°C
Ash Content (wt %)	1%	0.1
Moisture (wt %)	10	1

After the purification of crude glycerol, the purified glycerol dominantly with H_3PO_4. All the properties pH, density, organic matter, moisture content and ashes are similar with pure glycerol (Table 4). On the UV-Visible study of Purified glycerol is 0.0291 (least absorbance) for H_3PO_4 at λ 500 nm revealed that the crude glycerol (yellow-brown) is purified to glycerol (Colourless) (Table 5).

Table 5. *UV-Visible spectroscopy absorbance (λ 500) for different acids*

Acid	Absorbance (457 nm)
HNO_3	0.107
HCl	0.169
H_2SO_4	0.170
H_3PO_4	0.0291

The presence of various functional group were analysed by the FT-IR (Fig. 2).

In FT-IR spectra the peaks 1580 cm^{-1}, 1740 cm^{-1}, and 3050 cm^{-1} were absent showing confirming the removal of soap and other impurities (Fig. 1).

Conclusions

In this study, an integrated concept of producing methyl ester from the non-edible seeds of *M. oleifera* by the thermochemical conversion

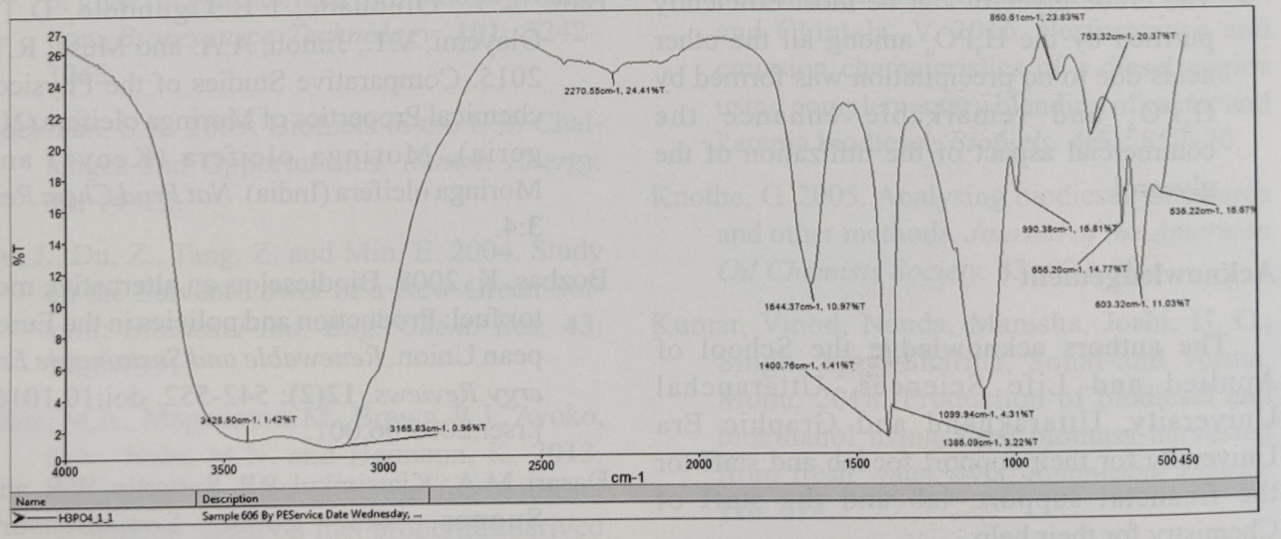

Fig. 2. *FT-IR Spectra of Purified Glycerol*

(TCC) and utilization of waste glycerol was investigated. From the above experimental observations, the following conclusion can be drawn:

- The higher yield of bio oil was achieved by the TCC as compared to the Soxhlet extraction.
- The presence of catalyst increases the rate and production of biodiesel.
- Biodiesel was synthesized from *M.oleifera* used as a feedstock and to make blends with conventional diesel fuel without engine modification.
- The percentage composition of M2+B5+D93 is used as a replacement to conventional diesel fuel among all the fuel compositions i.e. M5 + B10 + D85, M20 + B20+D60, M50 + B45 + D5 and M2 + B5+D93 was found to be a more suitable and sustainable blended eco-friendly fuel.
- The test result indicated that the obtained biodiesel and its blends have high oxidation stability, corrosion resistance, and high fluidity due to the addition of n- butanol.
- Purified Glycerol has excellent pour point as compared to other mineral oils.
- The crude glycerol can be most efficiently purified by the H_3PO_4 among all the other acids due to no precipitation was formed by H_3PO_4 and remarkable enhance the commercial aspect of the utilization of the glycerol.

Acknowledgement

The authors acknowledge the School of Applied and Life Sciences, Uttaranchal University, Uttarakhand and Graphic Era University for their support for lab and staff for the financial support, lab and the staff of Chemistry for their help.

Disclosure statement

No potential conflict of interest was reported by the authors.

References

Agarwal, A.K. and Rajamanoharan, K. 2009. Experimental investigations of performance and emissions of Karanja oil and its blends in a single cylinder agricultural diesel engine. *Applications Energy.* **86**: 106–12.

Arora, A., Patel, A., Pruthi, P.A. and Pruthi, V. 2016. Synergistic dynamics of nitrogen and phosphorous influences lipid productivity in Chlorella minutissima for biodiesel production. *Bioresour. Technol.* **213**: 79-87.

Atabani, A.E., Silitonga, A.S., Ong, H.C., Mahlia, T.M.I., Masjuki, H.H. and Badruddin, I.A. 2013. Non-edible Vegetable Oils: A critical evaluation of oil extraction, fatty acid compositions, biodiesel production, characteristics, engine performance and emissions production. *Renew Sust Energy Rev.* **18**: 211-45.

Aydin, H. and Ilkilic, C. 2010. Effect of ethanol blending with biodiesel on engine performance and exhaust emissions in a CI engine' *Applied Thermal Engineering.* **30**: 1199–204.

Bale, A.T., Olubuade, F.E.,Ogundele, D.T., Olayemi, V.T., Jimoh, A.A. and Musa, R.T. 2015. Comparative Studies of the Physicochemical Properties of Moringa oleifera (Nigeria), Moringa oleifera (Kenya) and Moringa oleifera (India). *Nat Prod Chem Res.* **3**:4.

Bozbas, K. 2008. Biodiesel as an alternative motor fuel: Production and policies in the European Union. *Renewable and Sustainable Energy Reviews.* **12(2)**: 542-552. doi:10.1016/j.rser.2005.06.001.

Dasari, M.A., Kiatsimkul, P.P., Sutterlin, W.R. and Suppes, G.J. 2005. Low-pressure hydrogenolysis of glycerol to propylene gly-

col. *Applied Catalysis A: General.* **281(1-2):** 225-231.

Demirbas, M. Fatih, 2011. Biofuels from algae for sustainable development. *Applied Energy.* **88**: 3473–3480.

Du, Z., Hu, B., Ma, X., Cheng, Y., Liu, Y., Lin, X., Wan, Y., Lei, H., Chen, P. and Ruan, R. 2013. 'Catalytic pyrolysis of microalgae and their three major components: carbohydrates, proteins, and lipids' *Bioresour. Technol,* **130**: 777–782.

Dwivedi, G. and Sharma, M. P. 2016. Investigation of oxidation stability of Pongamia biodiesel and its blends with diesel. *Egyptian Journal of Petroleum.* **25(1):** 15-20. doi:10.1016/j.ejpe.2015.06.005.

Foglia, T.A., Jones, K.C. and Phillips, J.G. 2005. Determination of Biodiesel and Triacylglycerol in Diesel Fuel by LC. *Chromatographia.* **66**: 115.

Franscisco, E.C, Neves, D.B., Lopes, E.J. and Franco, T.T. 2010. Microalgae as feedstock or biodiesel production: carbon dioxide sequestration, lipid production and biodiesel quality. *Biotechnol.* **85:** 395-403.

Hajek, Martin, Skopal, Frantisek, 2010. Treatment of glycerol phaseformed by biodiesel production. *Bioresource Technology.* **101**: 3242–3245.

Hoekman, S.K. 2009. Biofuels in the U.S. Challenges and Opportunities. *Renew. Energy.* **34:** 14–22.

Hu, J., Du, Z., Tang, Z. and Min, E. 2004. Study on the Solvent Power of a New Green Solvent: *Biodiesel Ind. Eng. Chem. Res.* **43**: 7928-7931.

Islam, M.A., Magnusson, M., Brown, R.J., Ayoko, G.A., Nabi, M.N. and Heimann, K. 2013. Microalgal species selection for biodiesel production based on fuel properties derived From fatty acid profiles. *Energies.* **6** : 5676–5702.

Jon, Van Gerpen, 2005. Biodiesel processing and production. *Fuel Processing Technology.* **86**: 1097–1107.

Joshi, H. C. and Kumar, B. 2016. Characteristics and composition of soyabean oil seed from India by Alkali - Catalysed transesterification and its potential as biodiesel feedstock. *Asian Journal of Chemistry.* **29**: 525–28.

Joshi, H.C. and Negi, Mahesh, 2017. Study the production and characterization of Neem and Mahua based biodiesel and its blends with diesel fuel: an optimum blended fuel for Asia. Energy Sources, Part A: Recovery, Utilization, and Environmental Effects. **39(17)**: 1894-1900.

Kafuku, G., Lam, M.K., Lee, K.T. and Mbarawa, Makeme, 2010. Heterogenous Catalysed biodiesel production from M. Oleifera oil. *Fuel Process Technol.* **9(11):** 1525-9

Kawashima Ayato, Matsubara, Koh, Honda, Katsuhisa, 2009. Acceleration of catalytic activity of calcium oxide for biodiesel production. *Bioresource Technology.* **100**: 696–700.

Khan Kahkashan, Kumar, Gitesh, Kumar, Amit, Sharma, P., Kumar, Suresh, Mandal, Chandan and Chintala, V. 2016. Performance and emission characteristics of a diesel engine using complementary blending of castor and karanja biodiesel. *Biofuels.* **4(5):** 859–70.

Knothe, G. 2005. Analysing biodiesel: Standards and other methods. *Journal of the American Oil Chemists Society.* **83:** 823–33.

Kumar, Vinod, Nanda, Manisha, Joshi, H. C., Singh, Ajay, Sharma, Sonal and Verma, Monu, 2018. Production of biodiesel and bioethanol using algal biomass harvested from fresh water river. *Renewable Energy.* **116**: 612.

Morton, J.F. 1991. The horseradish tree, Moringa

pterigosperma (Moringaceae). Aboon to arid lands. *Econ. Bot.* **45:**318–333.

Nanda, M.R., Yuan, Z., Qin, W., Poirier, Ma and Chunbao, X. 2014. Purification of Crude Glycerol using Acidification: Effects of Acid Types and Product Characterization. *Austin Chem Eng.* **1(1):** 1-7.

Pagliaro, M. 2013. Glycerol: The Platform Biochemical of the Chemical Industry. Simplicissimus. Book Farm, Palermo.

Priya and Brijesh, 2016. Studies on Purification of crude glycerol obtained as by-product from Biodiesel plant for conversion to value added products' *ICRAES,* **5(15),** 15-17.

Qi, D.H., Geng, L.M., Chen, H., Bian, Y.Z., Liu, J. and Ren, X.C. 2009. Combustion and performance evaluation of a diesel engine fuelled biodiesel produced from soybean crude oil. *Renewable Energy.* **34**: 2706–13.

Ramos, M.J., Fernandez, C.M., Casas, A., Rodriguez, L. and Perez, A. 2009. Influence of506 fatty acid composition of raw materials on biodiesel properties Bioresour. *Technol.* **507**, 261–268.

Sanchez, N., Sanchez, K. Encinar, J.M. 2015. Complete analysis of castor oil methanolysis to obtain biodiesel. *Fuel.* **147**: 95–99.

Sengupta, A. and Gupta, M.P. 1970. Studies on the seed fat composition of Moringaceae family. Fette, Seifen, *Anstrichm.* **72**:6–10.

Sousa, M., Dantas, I.T., Felix, A.K.N, Sant'Ana, H.B., Melo, V.M.M. and Gonçalves, L.R.B. 2014. Crude glycerol from biodiesel industry as substrate for biosurfactant production by Bacillus subtilis ATCC 6633. Brazilian *Archives of Biology and Biotechnology.* **57**: 295–301.

Tan, H.W., Aziz, A., Aroua, M.K. 2013. Glycerol production and its application as a raw material: a review. Renewable and Sustainable *Energy Reviews.* **27**: 118–127.

Thompson, J.C. and He, B.B. 2012. Characterization of crude glycerol from biodiesel production from multiple feedstocks. *Applied Engineering in Agriculture.* **22(2):** 261-265.

Wanga, Feng, Chang, Zhoufan, Duan, Peigao, Yan, Weihong, Yuping, Xu, Zhang, Lei, Miao, Juan, Fan, Yunchan, 2013. Hydrothermal liquefaction of Litsea cubeba seed to produce bio-oils. *Bioresource Technology.* **149** : 509–515.

Yunuskhan, T.M., Atabani, A.E., Anjum, Ahmad, Badruddin, Khayoon, M.S. and Triwahyono, S. 2014. Recent scenario and technologies to utilize non-edible oils for biodiesel production. *Renewable and Sustainable Energy Reviews.* **37**: 840–851.

(Received: 10 December 2019; Accepted: 14 June 2020)

Clay Research, Vol. 38, No. 2, pp. 83-89 (2019)

The Adhesive Strength of Fiber Reinforced Nano Clay/ Epoxy Matrix by Drag-Out Test

HISHAM MOHAMMED ALI HASAN[a,*] AND AHMED RASHEED MAJEED[b]

[a,*] *College of Education;* [b] *Physics Department, University of Al-Qadisiyah, 58001 Diwaniyah, P.O. Box 88, Iraq*

Abstract *- Clay nanoparticles are widely available and inexpensive natural resources with many features such as a large specific surface high mechanical.As a result, they have attracted more than special attention, in particular for the fiber reinforcement materials based onpolymers.The morphology and reactivity of clay nano-reinforcements can be set by varying the weight fraction of nanoclay in the epoxy matrix. The composite interfacial shear strength, which reflects the load transfer efficiency between the fiber and the matrix determined by drag–out test for glass fiber or carbon fiber reinforced nanoclay epoxy matrix at room temperature cured. clay-based with advanced mechanical properties relies on scale control molecular properties between clay and polymer matrix. The degree of layer exfoliation was shown by scanning electron microscopy and X-ray diffraction measurements.*

Keywords: Carbon fiber; Glass fiber; Interfacial shear strength; Nano-kaolinate; Single fiber drag-out test.

Introduction

Polymer composites have been used in a wide variety of industrial applications, such as automobiles, furniture, and construction for its advantages compared to metal materials, such as their lower cost, low density, chemical resistance, high strength-to-weight ratio, less damage to processing equipment, and good relative mechanical Properties (Ali *et al.,* 2016). Inorganic particles-polymer nanocomposites including clay mineral polymer nanocomposites (CPN) have attracted great attention during the past three decades because they often exhibit remarkable thermal, mechanical, and barrier properties. Compared with each individual constituent, these inorganic particles-polymer nanocomposites combine the best properties of both phases, yielding potential performance well beyond those of each individual constituent material (Jawaid *et al.,* 2016). Kaolinite is a dioctahedral 1:1 layer clay mineral with an idealchemical formula of $Al_2Si_2O_5(OH)_4$. Its layer was constituted by superposition and bonding of a Si tetrahedral sheet with an Al octahedralsheet. Although both montmorillonite and kaolinite possess plate-like structures, their cohesive energies between layers differ significantly. Kaolinite has no intercalated charge-balancing cations because of littleor no isomorphous substitution in the tetrahedral and octahedral sheets, unlike montmorillonite. Adjacent layers are linked by hydrogen bonds which makes delamination or the direct intercalation of kaolinite with inorganic and/or organic molecules much harderthan those of swelling (Tunney and Detellier, 1996; Wegst *et al.,* 2015). For the same reason, it is also hard to functionalize the surfaces of kaolinite leading to poor dispersion in polymer matrices. To solve these problems, a silylation reaction was performed on ground kaolinite and was successfully incorporated in the polymer without resorting to the intercalation of highly polar, small molecules in kaolinite under severe reaction

***Corresponding Author's Email :** houshammah@gmail.com
DOI:10.5958/0974-4509.2019.00005.6

conditions (Xia *et al.,* 2010). The effect of such a functionalized kaolinite on epoxy curing was also evaluated by Tao et al. (Tao *et al.,* 2014), who found that the addition of functionalized kaolinitecould decrease activation energy and accelerate the curing reaction of epoxy resin.

The study of the interaction between the fiber and the polymeric matrix in a composite plays an important role because it influences both the physical and mechanical properties of the final materials. In particular, the adhesion—that is the ability to transfer stresses across the interface is often related to a combination of different factors such as the interface thickness, the interphase layer, the adhesion strength, and the surface energy of the fibers (Pisanova *et al.,* 2001).

The mechanical behavior of reinforcement materials not only depends on the mechanical properties of the reinforcement and matrix but also on the adhesion between them. The adhesion often is regarded as the third phase in a composite material. It depends on whether or not the adhesion is related to an interface which influenced by the interaction between reinforcement and matrix (Teklal *et al.,* 2018).

Materials and Methods

Experimental procedure

Materials

E-glass,carbon fiber /epoxy/nanoclayare the nanostructured U-shape specimens used in this study. The resin polymer used as a matrix is low viscosity epoxy adhesive (SIKADUR® 52) with two parts, part A (Resin) and part B (Hardener) (Sika Australia Pty. Ltd.). The nanoclay particles used in this investigation are nanokaolinite $Al_2Si_2O_5(OH)_4$, 80 nm, the six U-specimens matrices of different weight fraction used are 0, 1, 3, 5, 7, 12 wt %, each specimen matrix has been reinforced once using glass fiber and once again using carbon fiber with fiber diameter 0.03 μm.

Specimen preparation

For preparation matrix resin, the nanokaolinite particles with different weight fraction are mixed by ultrasonic stirrer with epoxy resin (part A) for 90 min and then the mixture is stirred slowly with the hardener (part B) for 10 min, the nanoclay epoxy polymer poured in U-shaped polysiloxane specimen Figure 1. Where the E-glass or the carbon fibers with embedded lengths of 3 mm, 4 mm, 5 mm have been fixed. The U-shaped specimens were cured for a week at room temperature.

Tensile test

A tensile test and interfacial shear stress (Figure 1a, b, c) tests were performed using an Instron Universal

Testing Machine (ESM 301) the displacement drag-out rate were kept to 0.04 mm/min. Three specimens were tested for each composition. The maximum interfacial shear strength was

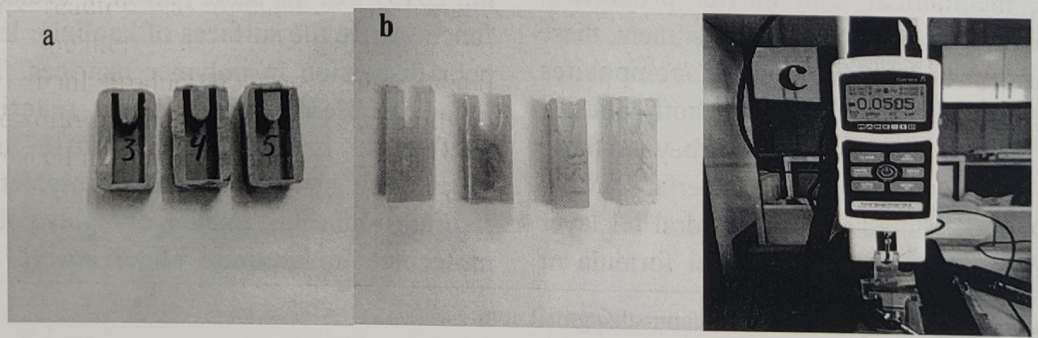

Fig. 1. (a) U-shaped polysilicone molds. (b) U-shaped specimens. (c) Instron ESM301

calculated by following the procedure described by Nuriela *et al.* (2005), The maximum pull-out force (P) were recorded and P_D is the component of (P) as shown in Figure 2.

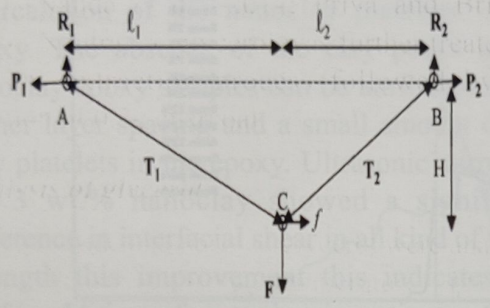

Fig. 2. *Force equilibrium for drag-out configuration.*

The interfacial shear stress calculated by equation (7) in reference 10 at the deviation point the maximum average interfacial shear stress at failure (π) using:

$$\tau = \frac{P_D}{(2\pi r_f l_e)} \qquad .. 1$$

Where r_f is the radius of the fiber and l_e is the length of a microbond specimen, the maximum average interfacial shear stress at failure for specimens.

Results and Discussions

The drag-out experimental data in Figures 3 and 4 shown in Table 1, the results were as the weight percentage of nanoclay increased, the interfacial shear strengths of the samples also increased as compared with pure epoxy matrix, the maximum increment by 3wt% in the shear strength when compared with other weight percentages. The decrease in interfacial shear strength was however less in specimen with nanoclay epoxy matrix in comparison to specimen with pure epoxy matrix and for all embedded lengths.

The important factors in determining good adhesive strength at the interface are the interface flaws and the surface energy of the reinforcement is close to or higher than the surface energy of the polymer matrix. This results in the substrate surface and the adhesive having strong force between them. If a substrate has low surface energy compared to the epoxy, then the epoxy matrix will be attracted to itself rather than to the reinforcement this characterized by having the epoxy bead up on the surface rather than spreading out and wetting the reinforced surface. To investigate the crystallographic structure of fiber-reinforced epoxy nanocomposites, XRD was carried out in a Labx, XRD-6000 shimsdzu diffractometer at a voltage of 40 kV and a current of 30 mA with CuKa radiation (λ= 1.5406 A^0), employing a scanning step size 0.02^0 in the 2è ranging from 5^0 to 80^0. The XRD results indicate an increase in d-spacing between the plateletsof nanoclay. The d-spacing of the inter-gallery

Table 1. *Maximum interfacial shear stress (ô) (MPa) calculated by equation (1) for different embedded lengths and nanoclay weight fraction.*

Specimen (l_e mm)	Interfacial shear strength (MPa)					
	Pure epoxy matrix	1wt% nanoclay epoxy matrix	3wt% nanoclay epoxy matrix	5wt% nanoclay epoxy matrix	7wt% nanoclay epoxy matrix	12wt% nanoclay epoxy matrix
Glass fiber $3l_e$	0.4609	2.155	2.5696	1.7499	1.72	0.6168
Glass fiber $4l_e$	0.0893	1.596	2.2239	1.9318	1.8223	0.609
Glass fiber $5l_e$	0.2723	1.8826	3.482	1.002	0.5835	0.3937
Carbon fiber $3l_e$	0.5493	1.2909	4.525	1.494	1.324	0.935
Carbon fiber $4l_e$	0.5359	3.607	5.0925	4.7443	3.6159	1.8185
Carbon fiber $5l_e$	1.6433	1.9994	2.6564	3.6937	3.4953	1.3543

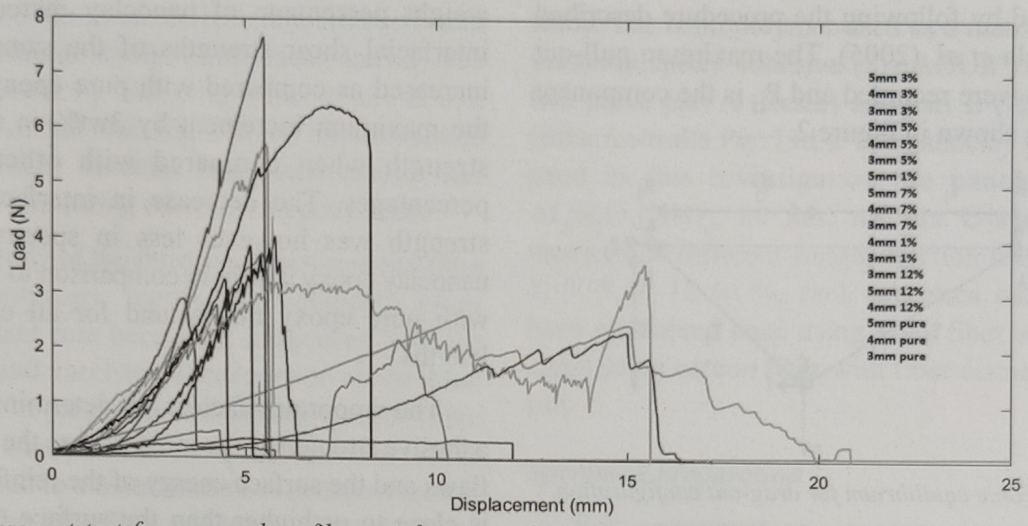

Fig. 3. *Drag-out test for epoxy glass fiber reinforcement for 3-mm, 4-mm, 5-mm embedded lengths and different nanoclay weight fraction.*

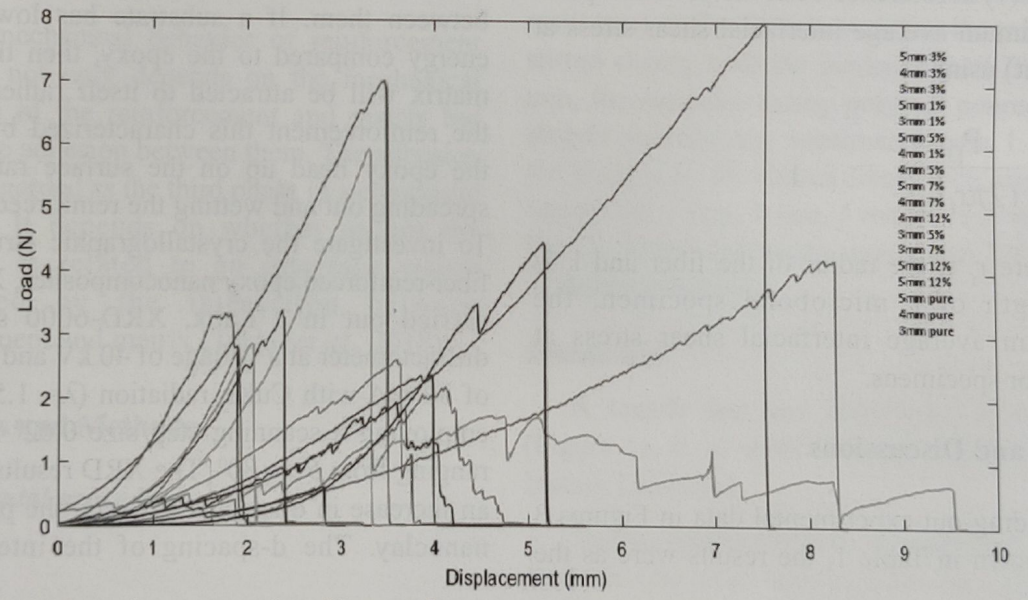

Fig. 4. *Drag-out test for epoxy carbon fiber reinforcement for 3-mm, 4-mm, 5-mm embedded lengths and different nanoclay weight fraction.*

spacing was determined using Bragg's Law. The X-ray diffraction for the pure and different weight fractions in figure 5 showed same peak pattern as in the pure epoxy, there was a little shift in peak position relative to the pure epoxy peak patterns, which indicatea change in the polymer network structure.

The d-spacing, Table 2 for the pure epoxy and nanoclay-epoxy matrix showed an increase of approximately 2.8% for nanoclay weight

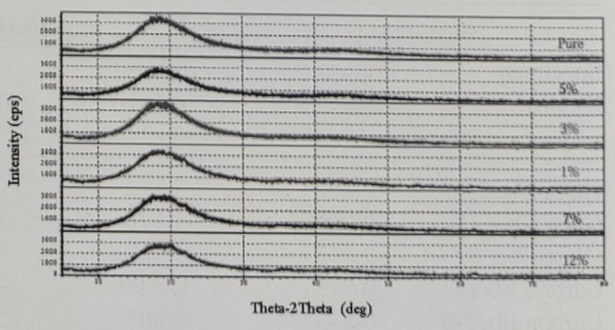

Fig. 5. *XRD patterns of pure epoxy matrix and epoxy – nanoclay matrix from 1 wt% to 12 wt %.*

fraction 1% and 3% and decreasing 5.99% for weight fraction 12%, the increases in the d-spacing allow the epoxy molecules to penetrate between the clay sheets to promote strong intercalation of the nanoclay platelets in the epoxy. The absence of the clay peaks in the nanoclay epoxy samples can be attributed to the higher layer spacing and a small amount of the clay platelets in the epoxy. Ultrasonic stirrer for the 3 wt.% nanoclay showed a significant difference in interfacial shear in all kind of fibers strength this improvement this indicates that 3wt% addition of nanoclay is optimum to get better adhesion.

Table 2. *X-ray diffraction parameters for the pure and nanoclay matrices.*

Specimen	2 Θ (deg.)	Intensity (cps)	d-space (nm)
pure	18.5872	198	0.476985
1%	18.1280	144	0.488963
3%	18.0681	205	0.490570
5%	18.5872	175	0.476985
7%	19.7835	168	0.448403
12%	19.8233	151	0.447512

When the silicate layers are completely and uniformly dispersed in a continuous epoxy polymer matrix, exfoliated nanocomposites are obtained. Exfoliated nanocomposites show greater phase homogeneity than intercalated nanocomposites. Each nano layer in an exfoliated nanocomposite contributes fully to interfacial interactions with the matrix. EDX measurements were performed with scanning electron microscope XFlash® 6 | 100 Energy Resolution: 133 eV (Mn Kα) at 100,000 cps, the elemental phases and chemical composition of nanoclay epoxy matrix was carried out, and the results shown in figure 6 are listed in Table 3.

EDX analysis reflected the composition of the hybrid organic-inorganic polymer composite, containing carbon, oxygen, silicon, aluminum, and magnesium, the nanoclay-epoxy chemical elements and its distributions. EDX show the presence of Al, Si and O elements in nanoclay, which is due to the clay phase (Alumina and Silica layered structure), further, EDX progress reports *permit the estimation* of the quantity of the elements in terms of atomic and weight percentages of all samples given in Table 3. The analysis shows an increase in C atom percentages for 3% weight percentage nanoclay over pure epoxythis due to the presence of long chains of epoxy in the sample. In the presence of Cloisite 30B in epoxy, Figure 6 shows the carbon and oxygen atom distributions on a specimen of epoxy with different nanoclay percentage. The EDX results shown in Table 3, regarding silicon, aluminum, and magnesium atom distributions, further support the observation of aggregates of

Table 3. *EDX analysis of pure epoxy matrix and epoxy – nanoclay matrix from 1 wt% to 12 wt%.*

Element	Epoxy pure	Epoxy – nanoclaywt%				
	0wt%	1wt%	3wt%	5wt%	7wt%	12wt%
C	55.10	61.95	64.37	57.23	52.95	49.60
N	13.29	5.65	4.52	3.74	3.68	3.60
O	31.61	17.28	14.83	17.46	17.18	15.08
Na	-	1.92	1.21	1.20	1.30	1.36
Mg	-	1.71	1.41	1.46	1.67	2.59
Al	-	2.52	3.93	4.72	5.98	7.43
Si	-	5.76	7.62	11.34	14.00	17.07
Cl	-	1.78	1.03	1.71	1.62	1.70
K	-	0.73	0.64	0.64	0.70	0.81
Ca	-	0.70	0.44	0.49	0.93	0.77
Total	100%	100%	100%	100%	100%	100%

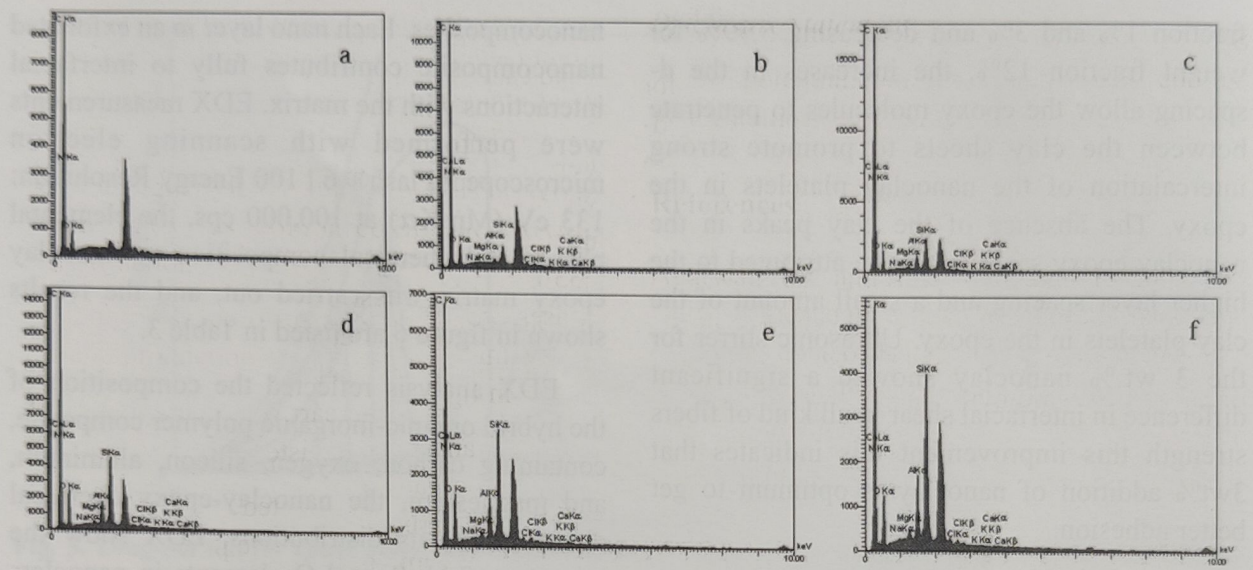

Fig. 6. *EDX graphs of (a) pure epoxy matrix, (b) 1% nano-clay epoxy matrix, (c) 3% nanoclay epoxy matrix,(d) 5% nanoclay epoxy matrix, (e) 7% nanoclay epoxy matrix, (f) 12% nanoclay epoxy matrix.*

silicate in the samples EDX analysis.

Conclusions

- Preparation methods for specimens allow the matrix to be in phase-separated, intercalated or exfoliated structure.
- The mechanical properties of the resulting nanocomposites are greatly improvedin comparison with pure polymer matrix to the homogeneous and fine dispersion of the sheetsnanoclay in the polymer matrix and strong interfacial interactions between these twoconstituents.
- The dispersion of clay particle in the epoxy matrix is dependent on the mixing time parameter. It is important that achieving evenly clay particle-dispersed nanocomposite as much as synthesizing exfoliated nanocomposite.
- The steady-state crack propagation values at interface of nanoclay filled epoxy composites were found to surpass the bulk polymer fracture energy.
- For matrix with 3 wt% nano clay the interfacial shear strength at fiber-matrix bonding strength was sufficiently high.

References

Ali, F., Ullah, H., Ali, Z. Rahim, F., Khan, F. and Rehman, Z.U. 2016. Polymer-clay Nanocomposites, Preparations and Current Applications: A Review. *Current Nanomaterials.* **1(2) :** 1-13.

Jawaid, M., Qaiss, A.K. and Bouhfid, R. 2016. *Nanoclay Reinforced Polymer Composites: Nanocomposites and Bionanocomposites.* Springer Singapore. [DOI: 10.1007/978-981-10-1953-1].

Nuriela, S., Katzb, A. and Wagnera, H.D. 2005. Measuringfiber-matrix interfacial adhesion by means of a 'drag-out' micromechanical test. *Composites*: *Part A*. **36**: 33–37.

Pisanova, E., Zhandarov, S., Mader, E., Ahmad, I. and Young, R.J. 2001. Three Techniques of Interfacial Bond Strength Estimation from Direct Observation of Crack Initiation and Propagation in Polymer–Fiber Systems. *Composites Part A*. **32**: 435–443.

Sika Australia Pty. Ltd. Material Safety Data Sheet, 55 Elizabeth Street (Locked Bag 482 BDC) Wetherill Park, NSW 2164, Australia. Downloaded from https://www.cwid.com.au/assets/uploads/18/productcatalogue/datasheets/SIKADUR 52.

Tao, Q., Su, L.N., Frost, R.L., Zhang, D., Chen, M.Y., Shen, W. and He, H.P. 2014. Silylation of mechanically ground kaolinite. *Clay Miner.* **49** : 559–568.

Teklal, F., Djebbar, A., Allaoui, S., Hivet, G., Joliff, Y. and Kacimi, B. 2018. A review of analytical models to describe pull-out behavior – Fiber/matrix adhesion. *Composite Structures* **201**(1): 791-815. [https://doi.org/10.1016/j.compstruct.2018.06.091].

Tunney, J.J. and Detellier, C. 1996. Chemically modified kaolinite grafting of methoxygroups on the interlamellar aluminol surface of kaolinite. *J. Mater. Chem.* **6**:1679–1685.

Wegst, U.G.K., Bai, H., Saiz, E., Tomsia, A.P., and Ritchie, R.O. 2015. Bioinspired structural materials. *Nat. Mater.* **14:** 23–36.

Xia, X., Zeng, X., Liu, J., and Xu, W. 2010. Preparation and characterization of epoxy/kaolinite nanocomposites. *J. Appl. Polym. Sci.* **118**: 2461–2466.

(Received: 10 December 2019; Accepted: 14 June 2020)

ACKNOWLEDGEMENT

Editorial Board greatly appreciate following reviewers:

Dr. Swapna Mukherjee, Kolkata, India

Dr. Shashi Prakash Dwivedi, Dehradun, India

Dr. Ruma Das, New Delhi, India

Dr. D.K. Pal, Nagpur, India

INSTRUCTIONS FOR CONTRIBUTORS

CLAY RESEARCH is the official publication of THE CLAY MINERALS SOCIETY OF INDIA and is published twice a year, in June and December. The Journal undertakes to publish articles of interest to the international community of ceramics, civil and petroleum engineering, clay mineralogy, crystallography, geochemistry, geology, material sciences, nanotechnology, pedology, petrochemical, petrology, pharmaceutical, physical and colloid chemistry, physics, soil science, and host of other kindred academic and industrial disciplines. It does not charge authors any fees for submission, and accept papers from authors irrespective of contributing author(s) nationality, race, gender and membership of the CMSI. Its publication profile of contributing authors, editors and reviewers is international. All submitted articles undergo double-blind peer-review process and editorial scrutiny before publication.

The articles published in Clay Research are indexed in Scopus, Google Scholar, CNKI Scholar, EBSCO Discovery, and Summon (ProQuest). The Clay Minerals Society of India (CMSI) is affiliated to the Clay Minerals Society and is a member of AIPEA (Association Internationale pour I'Etude des Argiles).

Paper (in English) in MS Word (2007 or above) format should be submitted through e-mail attachment to the "Chief Editor - Clay Research" at the <cedclayres@gmail.com>. Submission is an undertaking that the manuscript has not been published or submitted for publication elsewhere.

Manuscripts should not exceed sixteen typed (double spaced) pages including tables and illustrations. Only online submission of manuscript complete in all respect is accepted.

Form: Manusciprts should be typewritten, double spaced on white paper, with wide margins with page and lines numbered. Intending contributors should consult a recent issue of CLAY RESEARCH for the standard format and style. The manuscript should have the sections ABSTRACT, introductory portion (untitled), MATERIALS AND METHODS, RESULTS and DISCUSSION and REFERENCES.

Title page should contain manuscript title, full name(s) of author(s), address (es) of the institution(s) of the author(s), a short running title not exceeding 60 characters including spaces, footnotes if any to the title, and complete mailing address of the person to whom communications should be sent.

Abstract should be a condensation of the ideas and results of the paper. It should not exceed 250 words. Do not make reference to the literature in the abstract.

Tables should have the simplest possible column headings. Type each table on a separate page; indicate location in the text by marking in the margin of text page.

Figures should be self-illustrative, drawn with black India ink on tracing paper or white Board. The lattering should be large enough to permit size reduction to one Journal page column width (about 7.0 cm) without sacrificing legibility. **The original tracing should be submitted**. The size of the drawing should not exceed 24 × 17 cm. Give the numbered legend on a separate sheet, not on the figure itself. Data available in the tables should not be duplicated in the form of illustrations. Indicate the location of the figure in the text by marking in the margin of the page.

Photographs should be in the form of glossy prints with strong contrast. In photomicrographs, the scale in micron or other suitable unit should be drawn on the print. Give the numbered legend on a separate sheet. Indicate the location of the photograph in the text by making in the margin of the text page.

References should be cited in the text by the name(s) of author(s) if two or less, and year of publication. If there are more than two authors, give the name ofthe first author followed by *'et al'* and year. Full references giving author(s) and initial(s), year, title of paper, (journal, volume, number if paged separately), first and last pages should be listed alphabetically at the end of the paper. Journal title should be abbreviated in accordance with the World List of Scientific Periodicals and its sequences. Examples are

Grim, R.E., Bray, R.H. and Bradley, W.R. 1937. The mica in argillaceous sediments. *Am. Miner.* **22**:813-829.

Brindley, G.W. 1961. Chlorite minerals. In *(G.* Brown, Ed.) *The X-ray Identification and Crystal Structures of Clay Minerals,* Mineralogical Society, London, pp.242-296.

Theng, B.K.G. 1974. *The Chemistry of Clay Organic Reactions,* Adam. Hilger, London, 343 pp.

Reprints No free reprints are supplied to authors. Order for priced reprints should be sent when required by the Editor.

Clay Research

Vol. 38 **December 2019** **No. 2**

CONTENTS

Covid-19 and Nanoform Zinc Oxide Interaction: A Forcite Module of Materials Studio Software Study
R. Djefaflia, D. Lerari and K. Bachari .. 43

Clay Mineralogical and Geochemical Evidences of Lateritic Weathering at About 2.2 Ga Prior to the Evolution of Life on Earth
Rohit Kumar, Nandan Kumar and Pankaj Srivastava .. 56

Petrological Characterization of Residual Quartzites Associated With Kadavur Anorthosite Complex, Tamil Nadu, India
Kumar R. S., Asaimani S. Justine Antony K., Rajkumar P. and Aran Castro A. J. .. 63

Thermochemical Conversion of non-Food Feedstock of Moringa *oleifera* Seed Bio-Oil to the Biodiesel and its Blends with n- Butanol-diesel and Utilization of Glycerol Obtained as By-product
Harish Chandra Joshi, Jitendra Singh and Aishwarya Aggarwal .. 75

The Adhesive Strength of Fiber Reinforced Nano Clay/ Epoxy Matrix by Drag-Out Test
Hisham Mohammed Ali Hasan and Ahmed Rasheed Majeed .. 83

Printed at : Cambridge Printing Works, New Delhi-1100028, Cell Phone: +919811860113